Accepted Version
Preprint typeset using LaTeX style emulateapj v. 10/09/06

arXiv:0807.3744v1 [astro-ph] 23 Jul 2008

AGE DETERMINATION OF SIX INTERMEDIATE-AGE SMC STAR CLUSTERS WITH HST/ACS *

Katharina Glatt[1,2,3], Eva K. Grebel[3], Elena Sabbi[3,4], John S. Gallagher III.[2], Antonella Nota[4], Marco Sirianni[4], Gisella Clementini[5], Monica Tosi[5], Daniel Harbeck[2], Andreas Koch[6], Andrea Kayser[1], and Gary Da Costa[7]

Accepted Version

ABSTRACT

We present a photometric analysis of the star clusters Lindsay 1, Kron 3, NGC 339, NGC 416, Lindsay 38, and NGC 419 in the Small Magellanic Cloud (SMC), observed with the *Hubble Space Telescope* Advanced Camera for Surveys (ACS) in the F555W and F814W filters. Our color magnitude diagrams (CMDs) extend ∼3.5 mag deeper than the main-sequence turnoff points, deeper than any previous data. Cluster ages were derived using three different isochrone models: Padova, Teramo, and Dartmouth, which are all available in the ACS photometric system. Fitting observed ridgelines for each cluster, we provide a homogeneous and unique set of low-metallicity, single-age fiducial isochrones. The cluster CMDs are best approximated by the Dartmouth isochrones for all clusters, except for NGC 419 where the Padova isochrones provided the best fit. Using Dartmouth isochrones we derive ages of 7.5 ± 0.5 Gyr (Lindsay 1), 6.5 ± 0.5 Gyr (Kron 3), 6 ± 0.5 Gyr (NGC 339), 6 ± 0.5 Gyr (NGC 416), and 6.5 ± 0.5 Gyr (Lindsay 38). The CMD of NGC 419 shows several main-sequence turn-offs, which belong to the cluster and to the SMC field. We thus derive an age range of 1.2-1.6 Gyr for NGC 419. We confirm that the SMC contains several intermediate-age populous star clusters with ages unlike those of the Large Magellanic Cloud (LMC) and the Milky Way (MW). Interestingly, our intermediate-age star clusters have a metallicity spread of ∼0.6 dex, which demonstrates that the SMC does not have a smooth, monotonic age-metallicity relation. We find an indication for centrally concentrated blue straggler star candidates in NGC 416, while for the other clusters these are not present. Using the red clump magnitudes, we find that the closest cluster, NGC 419 (∼50 kpc), and the farthest cluster, Lindsay 38 (∼67 kpc), have a relative distance of ∼17 kpc, which confirms the large depth of the SMC. The three oldest SMC clusters (NGC 121, Lindsay 1, Kron 3) lie in the north-western part of the SMC, while the youngest (NGC 419) is located near the SMC main body.

Subject headings: galaxies: star clusters, — galaxies: Magellanic Clouds

1. INTRODUCTION

Star clusters are powerful tools for probing the star-formation history and the associated chemical evolution of a galaxy. As one of the closest star forming galaxies with star clusters covering a wide range of ages, the Small Magellanic Cloud (SMC) is a preferred location for detailed studies of this class of objects. The SMC is the only dwarf galaxy in the Local Group containing populous intermediate-age star clusters of all ages. The SMC appears to be part of a triple system together with the Large Magellanic Cloud (LMC) and the Milky Way (MW). Its star formation activity may be triggered by interactions with its companions (e.g. Yoshizawa & Noguchi 2003). The proximity of the SMC allows us to resolve individual stars in compact and massive star clusters of intermediate and old age, down to the sub-solar stellar mass regime.

The globular cluster (GC) system of the MW exhibits a range of ages between ∼10.5 and 14 Gyr (e.g., De Angeli et al. 2005) with the oldest populations belonging to the most ancient surviving stellar systems. In the Galactic halo, a "young" group of star clusters is found with Pal 1 being the youngest with an age of 8 ± 2 Gyr (Rosenberg et al. 1998). Theories explaining the origin of these so-called young halo clusters, consider them to have been captured by the MW (Buonanno et al. 1995), to have been formed during interactions between the MW and the Magellanic Clouds (Fusi Pecci et al. 1995), or to have been accreted from destroyed and/or merged dwarf satellites (e.g., Zinn 1993; Mackey & Gilmore 2004).

The star formation history of the LMC shows pronounced peaks that coincide with the times of possible past close encounters between the LMC, SMC and MW, indicative of interaction-triggered cluster formation (e.g., Girardi et al. 1995). In the LMC, two epochs of cluster formation have been observed that are separated by an "age gap" of about 4-9 Gyr (e.g., Holtzman et al. 1999; Johnson et al. 1999; Harris & Zaritsky 2001). In

---

* Based on observations made with the NASA/ESA Hubble Space Telescope, obtained at the Space Telescope Science Institute, which is operated by the Association of Universities for Research in Astronomy, Inc., under NASA contract NAS 5-26555. These observations are associated with program GO-10396.

[1] Astronomical Institute, Department of Physics and Astronomy, University of Basel, Venusstrasse 7, CH-4102 Binningen, Switzerland
[2] Department of Astronomy, University of Wisconsin, 475 North Charter Street, Madison, WI 53706-1582
[3] Astronomisches Rechen-Institut, Zentrum für Astronomie der Universität Heidelberg, Mönchhofstr. 12–14, D-69120 Heidelberg, Germany
[4] Space Telescope Science Institute, 3700 San Martin Drive, Baltimore, MD 21218
[5] INAF - Osservatorio Astronomico di Bologna, Via Ranzani 1, 40127 Bologna, Italy
[6] Department of Physics and Astronomy, University of California at Los Angeles, 430 Portola Plaza, Los Angeles, CA 90095-1547
[7] Research School of Astronomy & Astrophysics, The Australian National University, Mt Stromlo Observatory, via Cotter Rd, Weston, ACT 2611, Australia

the early epoch a well-established population of metal-poor ($\langle [Fe/H] \rangle \sim -2$) star clusters with comparable properties to Galactic halo clusters (Suntzeff et al. 1992; Olsen et al. 1998; Dutra et al. 1999) was formed. These clusters are as old as the oldest globular clusters in the MW and in the Galactic dwarf spheroidal companions (Grebel & Gallagher 2004). In a second epoch, a large population of intermediate-age clusters with ages less than 3-4 Gyr have developed.

In contrast, the SMC contains only one old GC, NGC 121, which is 2-3 Gyr younger than the oldest GC in the LMC and MW (Glatt et al. 2008) (Paper I). The second oldest SMC star cluster, Lindsay 1, has an age of 7.5 ± 0.5 Gyr, and since then compact populous star clusters have formed fairly continuously until the present day (e.g., Da Costa 2002). Furthermore, the intermediate-age clusters in the SMC might survive for a Hubble time, due to their high mass and the structure of the SMC (no bulge or disk to be passed) (Hunter et al. 2003; Lamers et al. 2005; Gieles et al. 2007).

The existing age determinations to this point have often been associated with large uncertainties. Stellar crowding, field star contamination and faintness of the main-sequence turnoffs made the measurement of precise ages difficult. These problems affect in particular ground-based data. Another difficulty is the large depth extent of the SMC which exacerbates the distance modulus-reddening degeneracy for each cluster. These uncertainties can affect the age determination considerably.

The capabilities of the Advanced Camera for Surveys (ACS) aboard the *Hubble Space Telescope* (HST) provide an improvement both in sensitivity (depth) as well as angular resolution, which is essential for reliable photometric age determinations in dense clusters. We present improved cluster ages and distance determinations for Lindsay 1, Kron 3, NGC 416, NGC 339, Lindsay 38, and NGC 419. This is part of a ground-based and space-based program to uncover the age-metallicity evolution of the SMC. Our space-based imaging data were obtained with HST/ACS and our ground-based spectroscopy was obtained with *Very Large Telescope* (VLT). We combine our photometric results with spectroscopic metallicity determinations to obtain a well-sampled age-metallicity relation.

The age-metallicity relation determined so far indicated that SMC clusters of similar age may differ by several tenths of dex in metallicity (Da Costa & Hatzidimitriou 1998). Previous studies provided ages and metallicities of SMC star clusters using a variety of techniques and telescopes (see § 7). Combining all published cluster ages for e.g. Kron 3 (5-10 Gyr) (Gascoigne 1966; Alcaino et al. 1996; Mighell et al. 1998b; Udalski 1998; Rich et al. 2000), we find a wide range of ages for some key star clusters depending on the method used for the determination.

Here we present the deepest available photometry with HST/ACS, which allows us to carry out the most accurate age measurements obtained so far. We determine the ages of these clusters utilizing three different isochrone models, which also yields distances. In the next Section we describe the data reduction procedure. In § 3 we present the color-magnitude diagrams (CMD) of the clusters and discuss their main features. In § 5 we describe our age derivation method and present our results. We give an estimate of the distances of our clusters long the line-of-sight in § 6 and present a discussion and a summary in Sections § 7 and § 8, respectively.

2. OBSERVATIONS AND REDUCTIONS

The SMC clusters Lindsay 1, Kron 3, NGC 339, NGC 416, Lindsay 38, and NGC 419 were observed with the HST/ACS between 2005 August and 2006 March (Table 1). The observations are part of a project (GO-10396; principal investigator: J. S. Gallagher, III) that is focused on cluster and field populations and the star formation history of the SMC.

The images were taken with the F555W and F814W filters, which closely resemble the Johnson V and I filters in their photometric properties (Sirianni et al. 2005). For Lindsay 1, Kron 3, NGC 416, NGC 339, and Lindsay 38 we discuss photometry from the *Wide Field Camera* (WFC), while for NGC 419 and for the center region of NGC 416 photometry from the *High Resolution Camera* (HRC) was used. The WFC images cover an area of $200'' \times 200''$ at each pointing with a pixel scale of $\sim$0.05 arcsec. The HRC images cover an area of $29'' \times 26''$ at each pointing with a pixel scale of $\sim$0.025 arcsec.

The data sets were processed adopting the standard Space Telescope Science Institute ACS calibration pipeline (CALACS) to subtract the bias level and to apply the flat field correction. For each filter, the short and long exposures were co-added independently using the MULTIDRIZZLE package (Koekemoer et al. 2002). Cosmic rays and hot pixels were removed with this package and a correction for geometrical distortion was provided. Because these mainly affect the faint stars we did not perform CTE corrections. The resulting data consist of one 40 s and one 1984 s exposure (1940 s for Lindsay 38) in F555W and one 20 s as well as one 1896 s exposure (1852 s for Lindsay 38) in F814W (Tab. 1). The HRC data of NGC 419 consist of 70 s and 1200 s exposure in F555W and 40 s and 1036 s exposure in F814W each.

The photometric reductions were carried out using the DAOPHOT package in the IRAF [9] environment on DRIZZLed images.

WFC: Saturated foreground stars and background galaxies were discarded by using the Source Extractor (Bertin & Arnouts 1996). Due to the different crowding and signal-to-noise ratio properties of the long and the short exposure, photometry involving point spread function (PSF) fitting was only performed on the long exposures. For the short exposures, we used aperture photometry, which turned out to yield smaller formal errors than PSF photometry (see also Paper I). The detection thresholds were set at 3 σ above the local background level for Lindsay 1, 1 σ for Kron 3 and 4 σ for NGC 339, NGC 416, and Lindsay 38 in order to detect even the faintest sources. The threshold levels were set based on the different crowding effects of the single clusters. The data reduction and photometry for the WFC images followed exactly the procedures outlined in Pa-

---

[9] IRAF is written and supported by the IRAF programming group at the National Optical Astronomy Observatories (NOAO) in Tuscon, Arizona. NOAO is operated by the Association of Universities for Research in Astronomy, Inc. under cooperative agreement with the National Science Foundation.

TABLE 1
Journal of Observations

Cluster	Date yy/mm/dd	Filter	Total Exposure Time (s)	R.A.	Dec.
Lindsay 1	2005/08/21	F555W	40.0	$0^h03^m53.19^s$	$-73^\circ28'15.74''$
			1984.0	$0^h03^m52.66^s$	$-73^\circ28'16.47''$
		F814W	20.0	$0^h03^m53.19^s$	$-73^\circ28'15.74''$
			1896.0	$0^h03^m52.66^s$	$-73^\circ28'16.47''$
Kron 3	2006/01/17	F555W	40.0	$0^h24^m41.64^s$	$-72^\circ47'47.49''$
			1984.0	$0^h24^m41.92^s$	$-72^\circ47'45.49''$
		F814W	20.0	$0^h24^m41.64^s$	$-72^\circ47'47.49''$
			1896.0	$0^h24^m41.92^s$	$-72^\circ47'45.49''$
NGC 339	2005/11/28	F555W	40.0	$0^h57^m47.40^s$	$-74^\circ28'26.25''$
			1984.0	$0^h57^m47.13^s$	$-74^\circ28'24.16''$
		F814W	20.0	$0^h57^m47.40^s$	$-74^\circ28'26.25''$
			1896.0	$0^h57^m47.13^s$	$-74^\circ28'24.16''$
NGC 416 (WFC)	2006/03/08	F555W	40.0	$1^h07^m53.59^s$	$-72^\circ21'02.47''$
			1984.0	$1^h07^m54.09^s$	$-72^\circ21'01.79''$
		F814W	20.0	$1^h07^m53.59^s$	$-72^\circ21'02.47''$
			1896.0	$1^h07^m54.09^s$	$-72^\circ21'01.79''$
NGC 416 (HRC)	2006/08/12	F555W	70.0	$1^h07^m58.76^s$	$-72^\circ21'19.70''$
			1200.0	$1^h07^m58.96^s$	$-72^\circ21'19.30''$
		F814W	40.0	$1^h07^m58.76^s$	$-72^\circ21'19.70''$
			1036.0	$1^h07^m58.96^s$	$-72^\circ21'19.30''$
Lindsay 38	2005/08/18	F555W	40.0	$0^h48^m57.14^s$	$-69^\circ52'01.77''$
			1940.0	$0^h48^m56.76^s$	$-69^\circ52'03.07''$
		F814W	20.0	$0^h48^m57.14^s$	$-69^\circ52'01.76''$
			1852.0	$0^h48^m56.76^s$	$-69^\circ52'03.07''$
NGC 419 (WFC)	2006/01/05	F555W	40.0	$1^h08^m12.53^s$	$-72^\circ53'17.72''$
			1984.0	$1^h08^m12.71^s$	$-72^\circ53'15.49''$
		F814W	20.0	$1^h08^m12.53^s$	$-72^\circ53'17.72''$
			1896.0	$1^h08^m12.71^s$	$-72^\circ53'15.49''$
NGC 419 (HRC)	2006/04/26	F555W	70.0	$1^h08^m17.93^s$	$-72^\circ53'03.60''$
			1200.0	$1^h08^m17.78^s$	$-72^\circ53'02.80''$
		F814W	40.0	$1^h08^m17.93^s$	$-72^\circ53'03.60''$
			1036.0	$1^h08^m17.78^s$	$-72^\circ53'08.80''$

per I, and for a detailed description we refer the reader to this paper.

HRC (NGC416, NGC419): The photometry was carried out independently in F555W and F814W. The detection threshold was set at 4 σ for both NGC 416 and NGC 419 above the local background level.

For those stars common in both filters, we first performed aperture photometry using an aperture radius of 2 pixels to avoid the diffraction ring. Due to the fact that the PSF does not vary on the HRC images, a PSF then was constructed by combining 10 bright and isolated stars that were uniformly distributed over the entire image. The PSF photometry was then carried out. The objects found in both images were cross-identified and merged with a software package written by P. Montegriffo (private communication).

A spatial projection of the clusters' location towards the SMC (*red circles*) is shown in Figure 1 superimposed on a star map of the SMC generated using the point source catalog of the Small Magellanic Cloud Photometric Survey (Zaritsky et al. 2002) for stars V<16.5 mag. Additionally, we show the location of the eight intermediate-age star clusters (*blue crosses*), which we will discuss in § 7.

We show the photometric errors assigned by DAOPHOT for Kron 3 in Figure 2 as these are representative of our WFC data. The formal photometric errors remain negligible over a wide range of magnitudes for stars measured on the short exposures. Photometry obtained with aperture photometry on the long exposure yields smaller errors for stars brighter than $m_{555,814} \sim 22$ mag than with PSF photometry. In Kron 3, all brighter stars in the long exposures down to $m_{555} < 18.5$ mag and $m_{814} < 18.7$ mag are saturated. For stars brighter than $m_{555,814} = 20$ mag, the short exposure sample (*blue dots*), in the interval between $21.8 < m_{555,814} < 20$ mag the long exposure aperture photometry sample (*red dots*) and for stars fainter than $m_{555,814} = 21.8$ mag the long exposure PSF photometry sample (*black dots*) was used. We determined the cuts between the samples based on the m_{555} data and adopted the same value for m_{814} so as to avoid a color slope associated with this division.

For our study, we rejected all stars with a σ error larger than 0.2 mag and a DAOPHOT sharpness parameter $-0.2 \leq s \leq 0.2$ in both WFC and HRC filters. The resulting color-magnitude diagrams (CMD) of Lindsay 1, Kron 3, NGC 339, NGC 416, Lindsay 38, and NGC 419 are shown and discussed in the following Section.

3. THE COLOR-MAGNITUDE DIAGRAMS

All the CMDs of our six clusters show a well-populated main-sequence (MS), and clearly defined sub-giant and red-giant branches (SGB and RGB, respectively). The asymptotic giant branch (AGB) is less tightly defined, but clearly present in all cases, and especially evident in

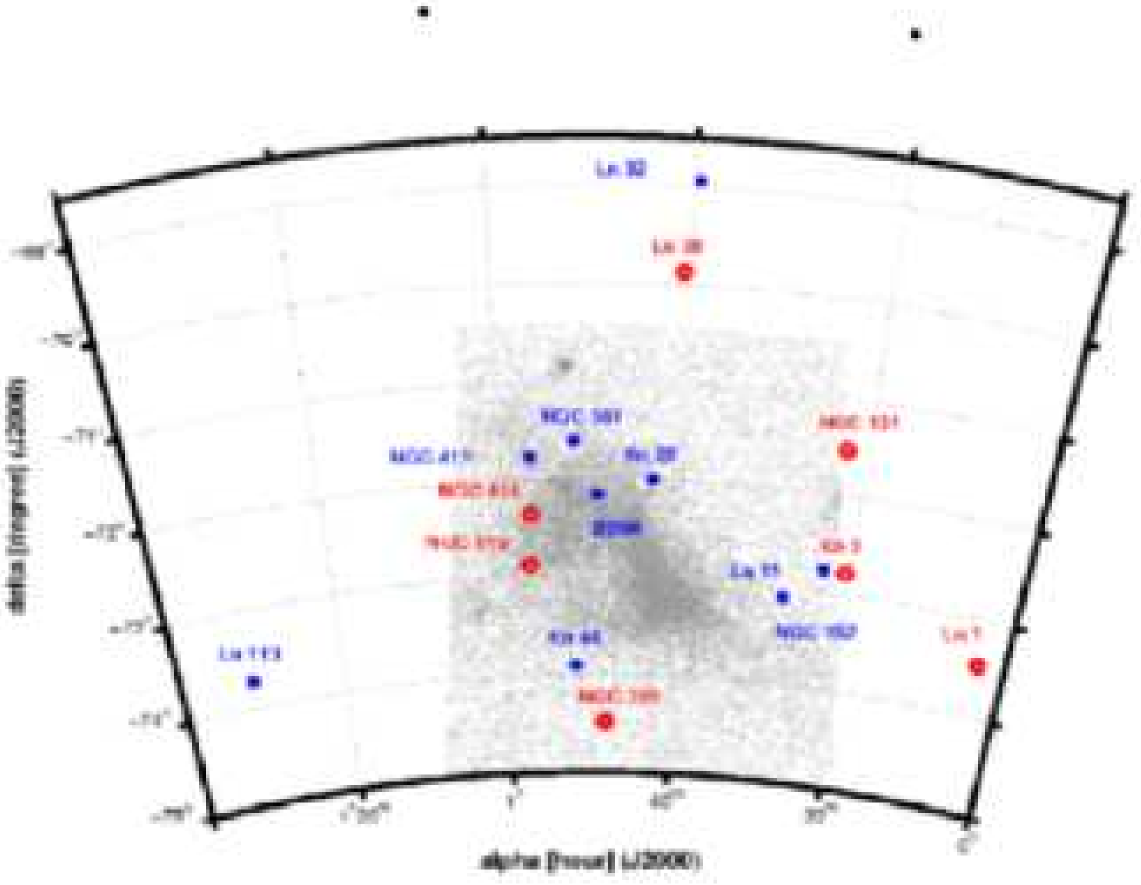

FIG. 1.— Spatial Distribution in 2D of our cluster sample (red circles). The location of eight additional SMC clusters, for which reliable ages from the literature are available, is shown (blue crosses). We obtain a complete sample of all intermediate-age and old SMC star clusters (see § 5), which we will discuss in § 6 and 7. One of the clusters, Lindsay 116, lies outside the coordinate boundaries of the Figure. The cluster locations are shown superimposed on a star map of the SMC generated using the point source catalog of the Small Magellanic Cloud Photometric Survey (Zaritsky et al. 2002) for stars with V<16.5 mag.

NGC 416 (Fig. 9). We define the main-sequence turnoff-point (MSTO) to represent the bluest point on the observed ridgeline. The data allow us to carry out the most accurate age measurement obtained so far (see Section 5), while also deriving improved distances. Lindsay 1, Kron 3, NGC 339, NGC 416, and Lindsay 38 appear to be single-age, simple stellar population objects, while the WFC data of NGC 419 shows multiple turnoff-points. For this reason we will discuss this cluster in greater detail in a separate paper (Sabbi et al. 2008, in preparation).

The CMDs show no obvious evidence for Galactic foreground contamination due to the high Galactic latitude of the SMC (e.g., Ratnatunga & Bahcall 1985). However, we find significant SMC field star contamination in the CMDs of Kron 3, NGC 339, NGC 416, and also in the HRC CMD of NGC 419. Field stars naturally are more problematic in CMDs of clusters near the SMC main body. For all clusters we give the magnitude of the MSTO, the red clump, and the red bump in Table 2. For the red clump and the red bump the mean magnitude was calculated by averaging the magnitudes of all clump and bump stars respectively and finding the maximum of each luminosity function.

For Kron 3 and Lindsay 38 no red bump was found. The red bump is a feature predicted by stellar evolution models, which imply that the luminosity of the RGB bump is dependent on the metallicity and age of the cluster. The failure to identify a red bump in the CMD of Lindsay 38 is due to its sparseness. The CMD of Kron 3, however, is well-populated, but despite sufficient statistics a red bump is not present, for which we have no physical explanation. In the CMDs of Lindsay 1, Kron 3, and NGC 339 a gap on the RGB at ∼20 mag is visible. For Lindsay 1 and Kron 3 this feature is artificial due to the cuts in photometric errors and sharpness we applied. However, for NGC 339 the gap appears to be real (see § 3.3).

3.1. *Lindsay 1*

The populous cluster Lindsay 1 (Lindsay 1958) is the westernmost known cluster in the SMC and lies around 3.5° west of the bar. Lindsay 1 is the second oldest star cluster in the SMC after NGC 121 (e.g., Paper I). The color-magnitude diagram (CMD) of Lindsay 1 is presented in Figure 3. The CMD reaches ∼3 mag

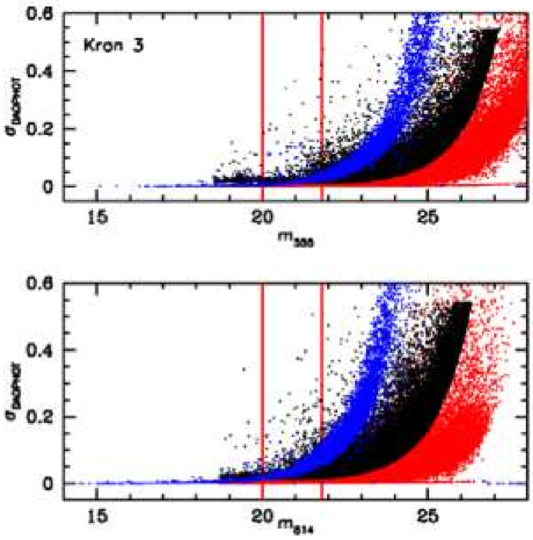

FIG. 2.— Photometric errors assigned by DAOPHOT to stars on the short (blue dots), and on the long (aperture photometry: red dots, PSF photometry: black dots) exposures for the cluster Kron 3. Stars brighter than ∼18.5 mag in the long F555W exposure and brighter than ∼18.7 mag in the long F814W exposure are saturated and are therefore not shown. The samples of the short, and the long exposures measured with aperture photometry and PSF photometry are combined at 21.8 mag and $m_{555} = 20$ mag (indicated by the thin vertical lines). For the F814W exposures we chose the same magnitude value in order to avoid introducing a color slope in the color-magnitude diagram of the resultant data set.

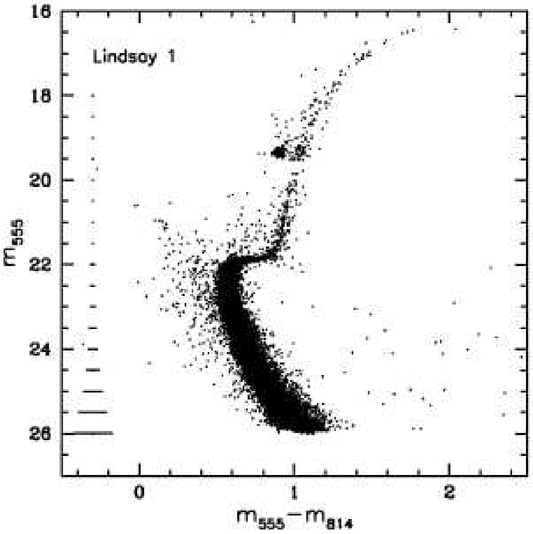

FIG. 3.— CMD of Lindsay 1 and its surroundings. Only stars with good photometry ($\sigma \leq 0.2$ mag and $-0.2 \leq$ sharpness ≤ 0.2) are shown; 15,321 stars in total. Representative errorbars (based on errors assigned by DAOPHOT) are shown on the left for the m_{555}-m_{814} color.

deeper than the previous deepest available photometry (Mighell et al. 1998b; Alcaino et al. 2003). Lindsay 1 is located in a low-density area outside the main body of the SMC (see Fig. 1). Therefore we find only little field star contamination by younger populations near Lindsay 1.

In Figure 4 we display the CMD for the stars in the center region of Lindsay 1. The location of the cluster center was visually estimated. All stars within a radius of 45" were selected to create the center sample. Most of the field contamination has vanished. Given the width of our MS, we cannot infer any information on the presence and percentage of unresolved binary systems.

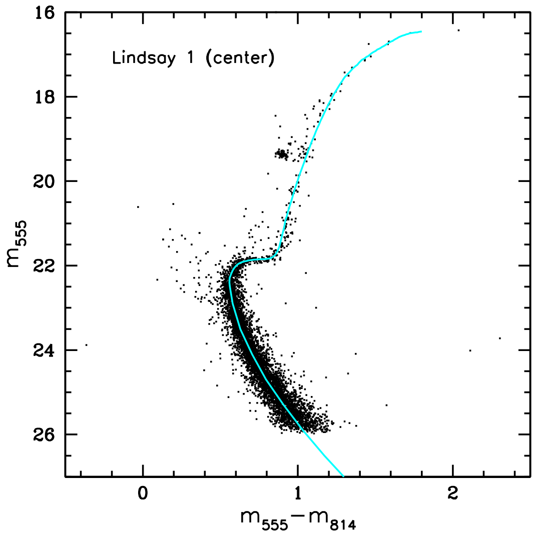

FIG. 4.— CMD of the central region of Lindsay 1. All stars within a radius of 45" were selected. We used this CMD for the determination of a representative color-magnitude ridgeline (cyan line) of Lindsay 1. This CMD contains 5,561 stars.

We find a well-populated red clump at a mean magnitude of $m_{555} = 19.36 \pm 0.04$ mag. Our value is in excellent agreement with the horizontal branch magnitude found by Sarajedini et al. (1995); Alves & Sarajedini (1999); Rich et al. (2000); Crowl et al. (2001, and Alcaino et al.(2003)). Obviously, Lindsay 1 is not old enough to have developed an extended red horizontal branch, which in itself is already a strong indication that Lindsay 1 is younger than NGC 121. We refer to Salaris & Girardi (2002) who study the behavior of the red clump as a function of age.

The red clump of Lindsay 1 is ∼0.35 mag brighter in F555W than that of NGC 121. The luminosity difference may imply that Lindsay 1 is closer than NGC 121 along the line-of-sight, which actually seems to be the case (see § 6). Adopting the absolute red clump magnitudes given by Girardi & Salaris (2001), and the reddening values from the Schlegel maps (Schlegel et al. 1998) of $E_{B-V} = 0.03$ mag, we find an absolute red clump magnitude difference between NGC 121 and Lindsay 1 of $\Delta M^{RC}_{m555} \sim 0.28$ mag. Therefore, the feature seen in Lindsay 1, should be considered a red clump and not a red horizontal branch.

The gap on the RGB at $m_{555} \sim 19.8$ mag is an artificial feature due to small number statistics resulting from our photometric selection (only photometry with $\sigma < 0.2$ mag and $-0.2 \leq s \leq 0.2$ is shown).

3.2. *Kron 3*

Kron 3 lies well outside the main SMC body, about 2° west of the bar. The cluster was first cataloged by Shapley & Wilson (1925), and it is number 3 in Kron's (1956) catalog of SMC star clusters. The highly populated CMD of Kron 3 is presented in Figure 5. The CMD reaches ∼2 magnitudes deeper than the previous deepest available photometry (Rich et al. 2000).

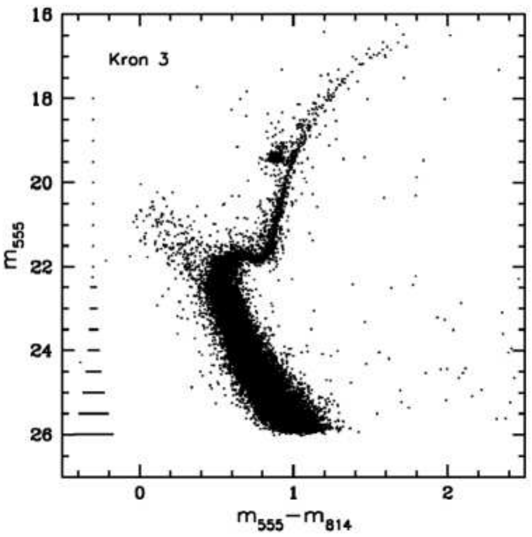

Fig. 5.— CMD of Kron 3 and its surroundings. Only stars with good photometry ($\sigma \leq 0.2$ mag and $-0.2 \leq$ sharpness ≤ 0.2) are shown; 30,264 stars in total. Representative errorbars (based on errors assigned by DAOPHOT) are shown on the left for the m_{555}-m_{814} color.

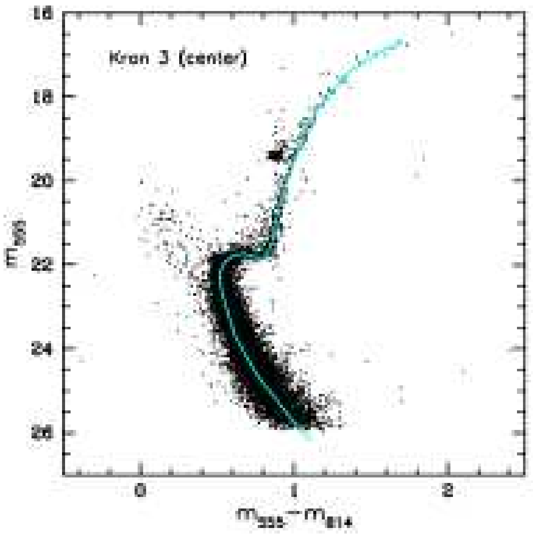

Fig. 6.— CMD of the central region of Kron 3. All stars within a radius of 40" were selected. We used this CMD for the determination of a representative color-magnitude ridgeline (cyan line) of Kron 3. This CMD contains 13,584 stars.

Field star contamination is visible along an extension of the main-sequence, towards brighter and bluer objects than at the cluster's MSTO. However, the cluster center is not affected by crowding, even though the center region is very dense.

In Figure 6 we display the CMD for the stars within 40" of the center of Kron 3. From the width of the MS, we cannot draw any conclusions about the presence of unresolved binary systems. The aforementioned traces of field contamination are still visible.

3.3. *NGC 339*

NGC 339 is located outside the SMC main body, around 1° south of the bar. The resulting CMD is shown in Figure 7, which reaches ∼2 magnitudes deeper than the previous deepest available photometry, published by Rich et al. (2000).

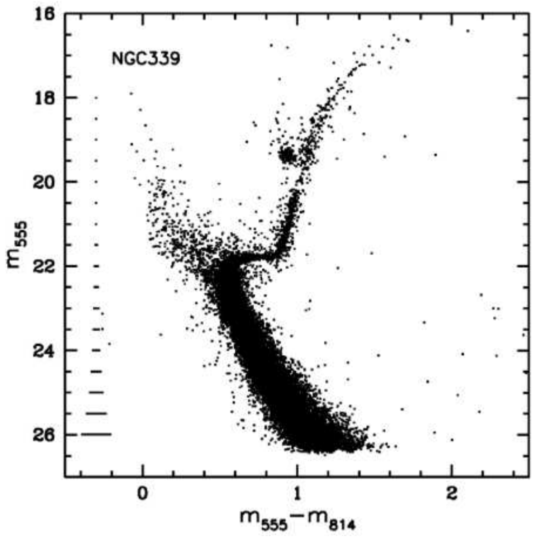

Fig. 7.— CMD of NGC 339 and its surroundings. Only stars with good photometry ($\sigma \leq 0.2$ mag and $-0.2 \leq$ sharpness ≤ 0.2) are shown; 29,304 stars in total. Representative errorbars (based on errors assigned by DAOPHOT) are shown on the left for the m_{555}-m_{814} color.

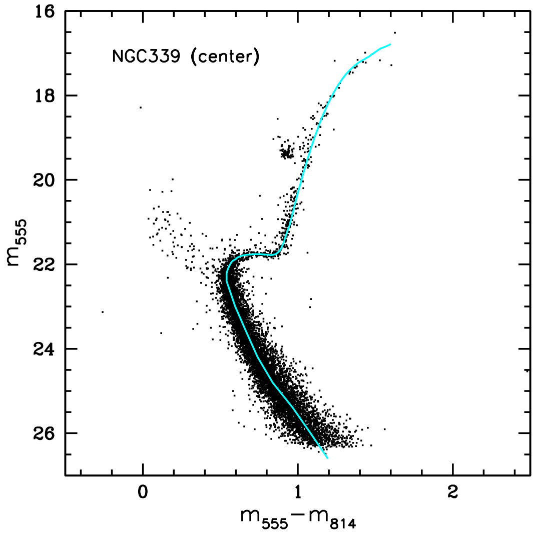

Fig. 8.— CMD of the central region of NGC 339. All stars within a radius of 35" were selected. We used this CMD for the determination of a representative color-magnitude ridgeline (cyan line) of NGC 339. This CMD contains 8,555 stars.

The SMC field is present along the luminous extension of the main-sequence. The cluster center is fully resolved and not affected by crowding since this is a very low density cluster. All features in our CMD are well defined. We cannot infer any information on unresolved binary systems due to the width of our MS. Unlike for the other clusters in our sample, the gap on the RGB at $m_{555} \sim 20$ mag is not an artificial feature. It is visible in both the single short and long exposures and has also been found in other SMC clusters, e.g. NGC 288 (Bellazzini et al. 2002).

To create the center sample, all stars within a radius of 35" around a visually estimated center were selected

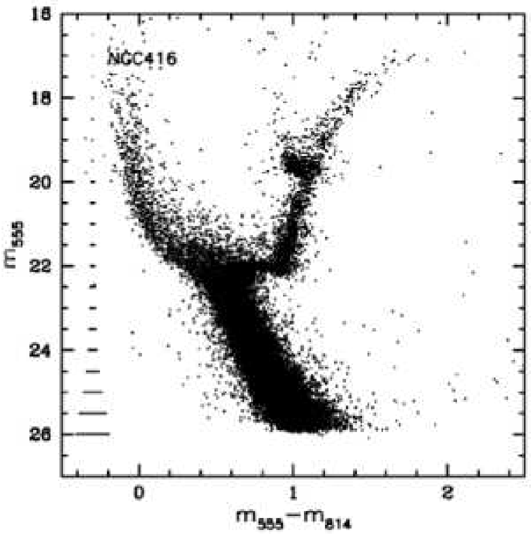

FIG. 9.— CMD of NGC 416 and its surroundings. Only stars with good photometry ($\sigma \leq 0.2$ mag and $-0.15 \leq$ sharpness ≤ 0.15) are shown; 18,764 stars in total. Additionally, we discarded all stars located within a radius of 15" around the cluster center, due to the high density of the cluster center and the resulting insufficient photometry. Representative errorbars (based on errors assigned by DAOPHOT) are shown on the left for the m_{555}-m_{814} color.

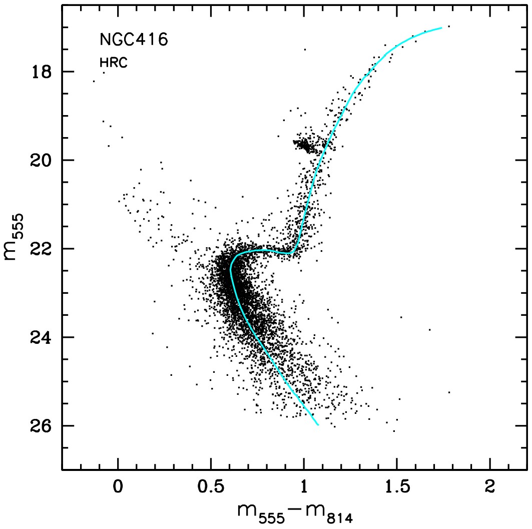

FIG. 10.— CMD of the HRC data of the center region of NGC 416. We used this CMD for the determination of a representative color-magnitude ridgeline (cyan line) of NGC 416. This CMD contains 4,992 stars.

and displayed in Figure 8. The SMC field is still clearly visible, which was expected due to the location of the cluster close to the SMC main body.

3.4. *NGC 416*

The cluster NGC 416 is located in the wing of the SMC. This part of the SMC is characterized by an increased stellar density that may represent a tidal extension towards the LMC. Due to the location of NGC 416 in the wing of the SMC, we expect a very rich CMD with strong SMC field star features. Our resulting CMD (Fig. 9) indeed presents a densely populated MS, SGB, RGB, AGB and red clump as well as more luminous blue MS and blue loop stars stars that belong to younger SMC field populations. The RGB is also broadened by SMC field stars and is not as narrow as in the other clusters in our sample. About 0.1 mag offset to the blue of the RGB, we find a very well-populated AGB.

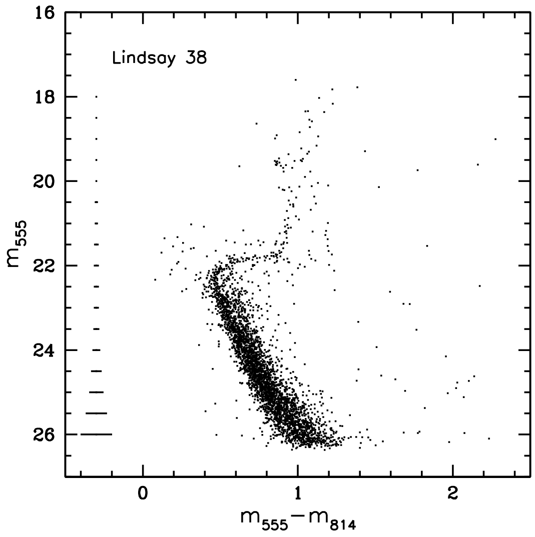

FIG. 11.— CMD of Lindsay 38 and its surroundings. Only stars with good photometry ($\sigma \leq 0.2$ mag and $-0.2 \leq$ sharpness ≤ 0.2) are shown; 3,716 stars in total. Representative errorbars (based on errors assigned by DAOPHOT) are shown on the left for the m_{555}-m_{814} color.

To obtain the final CMD we combine the HRC and the WFC photometry and discard the overlapping center region from the WFC catalog. For the WFC catalog, we only use PSF photometry of the long exposures and aperture photometry of the short exposures, because aperture photometry could not resolve single stars in the dense center region. The high density of the cluster center made it very difficult to find bright and isolated stars for the PSF sample in the cluster center. For the HRC data the long exposure images provided the better photometric quality. Therefore we do not include the short exposures in our final HRC catalog.

In Figure 10 we display only the HRC data of the center region of NGC 416, which was used for the ridgeline fit. The CMD is still densely populated and all cluster features are clearly outlined. Interestingly, the RGB of NGC 416 is still broadened by contaminating field stars. The main-sequence is well defined until ~24 mag and fades out for fainter magnitudes. A number of younger stars of the SMC field are still visible above the MSTO.

3.5. *Lindsay 38*

Lindsay 38 is located about 3.3° north of the bar and is among the outermost SMC clusters. Piatti et al. (2001) published the first and as yet only CMD of Lindsay 38. Our resulting CMD of the custer and its surroundings is shown in Figure 11. Our CMD reaches ~3 mag deeper than the CMD presented by Piatti et al. (2001), which was obtained from ground-based photometry. The cluster is very sparse and we identify only 3,716 candidate member stars.

In Figure 12 we show the CMD for the center sample. We selected stars within a radius of 70" around a visually estimated center location. The radius is almost twice as large as for the other clusters, due to the sparseness of the cluster.

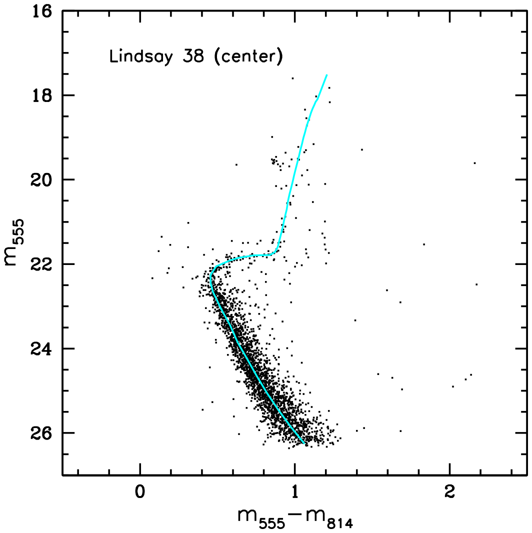

FIG. 12.— CMD of the central region of Lindsay 38. All stars within a radius of 70" were selected. We used this CMD for the determination of a representative color-magnitude ridgeline (cyan line) of Lindsay 38. This CMD contains 1,151 stars.

The MS and the SGB are nevertheless well defined. Only a few stars populate the upper RGB, but the red clump is clearly visible.

3.6. *NGC 419*

Like NGC 416, the cluster NGC 419 is located in the wing of the SMC. For this cluster, we show in this paper only the HRC data, and will discuss and analyze the full CMD in a separate paper due to its complexity. The CMD reaches ~2 mag deeper than the previous deepest available photometry, published by Rich et al. (2000).

Figure 13 displays our CMD of NGC 419, the youngest cluster in our sample. Only long exposure PSF photometry was used. The upper MS is rather broad and densely populated. The CMD reaches ~4.5 mag below the MSTO, but due to shorter exposure times and crowding, the MS becomes less densely populated at fainter magnitudes. The tip of the extended turn-off region lies at m_{555} ~20 mag, and more than one MSTO appear to be visible. For stellar populations in the corresponding age range (~1-1.6 Gyr), the hydrogen-shell burning phase lasts only for a short time (~70 Myr), which explains the sparse SGB (Schaller et al. 1992).

At m_{555} ~21.5 mag and $m_{555} - m_{814}$ ~ $0.5 - 0.9$ mag in the CMD we find ~30 SMC field stars, which may belong to an older MSTO. Mackey et al. (2008) (see also Mackey & Broby Nielsen 2007) discovered the only two star clusters in the LMC known to have a double MS, NGC 1846 and NGC 1806, which both have similar metallicities of about Z = 0.0075. The CMDs look very similar to NGC 419. Padova isochorones were used to determine the ages of NGC 1846 and NGC 1806 and yielded ages of 1.6 and 1.9 Gyr for both NGC 1846 and NGC 1806.

In Figure 14 we show the CMD with the derived ridgeline. At 19.41 ± 0.12 mag we find the vertically extended red clump. Below the red clump, ~0.2 mag fainter and ~0.1 mag in color to the blue, we find parts of a second red clump population at 19.53 ± 0.17 mag. For the old globular cluster NGC 121, we found the red clump at 19.71 ± 0.03 mag. Therefore we speculate that these fainter stars belong to a red clump of the old SMC field star population. If the luminosity difference (0.12 mag) between the two putative red clump populations were primarily due to distance (not age), then the distance d between the two populations can be calculated. We obtain δd = 4 pc.

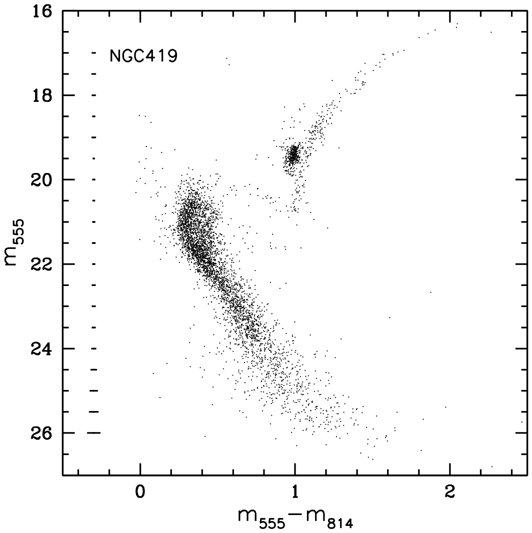

FIG. 13.— CMD of NGC 419 from the HRC images. Only stars with good photometry ($\sigma \leq 0.2$ mag) are shown; 4543 stars in total. Representative errorbars (based on errors assigned by DAOPHOT) are shown on the left for the m_{555}-m_{814} color.

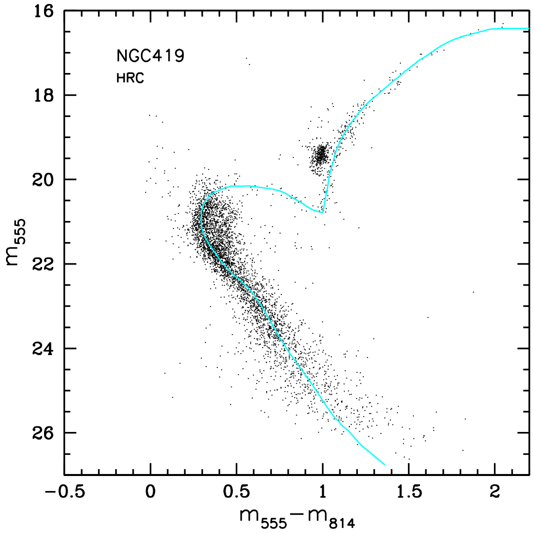

FIG. 14.— CMD of the central region of NGC 419. The derived fiducial ridgeline is shown as the cyan line.

The MSTO is located at 21.4 ± 0.1 mag and 0.41 ± 0.05 mag. We have to be cautious with the reliability of the determined MSTO, because as we will see in § 5.6 the isochrone models describe a hook-like feature past the MSTO, which is not visible in our CMD. This phase is traversed quite rapid (~27 Myr) for stars with ages between 1 and 1.6 Gyr (Schaller et al. 1992). This short phase lifetime is likely the reason why the hook is not visible.

4. BSS CANDIDATES

TABLE 2
Observational data

Cluster	$m_{555,TO}$ mag	$m_{555,Bump}$ mag	$m_{555,RC}$ mag
NGC 121	22.98 ± 0.05	19.52 ± 0.04	19.71 ± 0.03
Lindsay 1	22.36 ± 0.05	19.25 ± 0.05	19.36 ± 0.04
Kron 3	22.40 ± 0.05	-	19.46 ± 0.03
NGC 339	22.30 ± 0.05	19.27 ± 0.04	19.38 ± 0.08
NGC 416	22.44 ± 0.05	19.65 ± 0.06	19.70 ± 0.07
Lindsay 38	22.36 ± 0.05	-	19.60 ± 0.05
NGC 419	21.40 ± 0.10	18.86 ± 0.12	19.41 ± 0.12

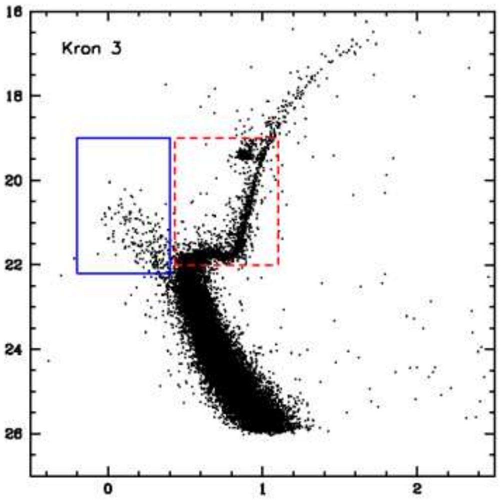

Fig. 15.— CMD of Kron 3 with displayed sample selection for the BSS sample (solid lines) and the cluster sample (dashed lines) including SGB, lower RGB, and red clump.

The stars blueward of and above the cluster MSTO are blue straggler star (BSS) candidates. In the same region often stars of the surrounding younger field population of the host galaxy are located. Knowledge of the BSS population of clusters is of interest with respect to constraining the binary fraction in these objects and with regard to understanding the formation mechanism of the BSS themselves (e.g., Bailyn 1995). BSS have been detected in a wide range of cluster types including very young, populous Magellanic Cloud clusters (e.g., Grebel et al. 1996), and old globular clusters (e.g., Ferraro et al. 2003). Carraro et al. (2008) showed for three open Galactic clusters that BSS are centrally concentrated when comparing the CMDs of the clusters and the surrounding field as one would expect for populations associated with a cluster. These authors re-emphasized the problem of field star contamination when trying to photometrically identify BSS.

Our ACS data do not cover fields adjacent to the clusters. Therefore, we calculated the projected distance from the cluster center for each BSS candidate. We then constructed a cumulative distribution of the number of blue stragglers as a function of projected radius. We have selected the BSS candidates by defining a region above the cluster main-sequence turnoff in the CMDs. We show the sample selection in the CMD of Kron 3 in Figure 15 as a representative example.

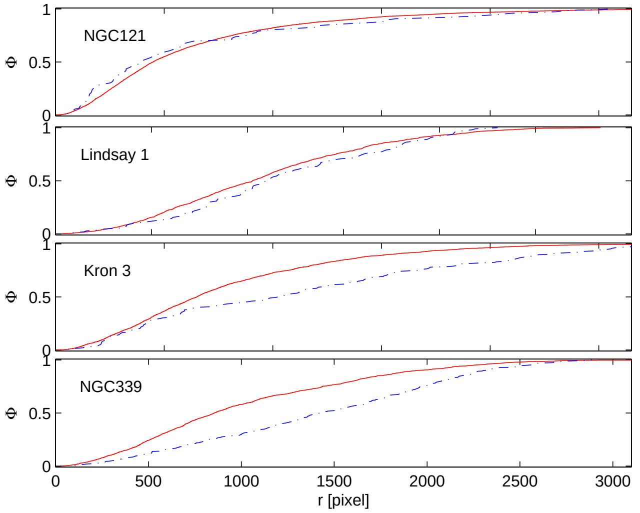

Fig. 16.— Cumulative radial distributions of blue straggler candidates as a function of projected radius for the clusters NGC 121, Lindsay 1, Kron 3, and NGC 339. The solid line represents the 'cluster sample' including the SGB, RGB, and red clump. The dashed line represents the stars found in the BSS region. The uppermost panel shows the distributions of NGC 121 for comparison, because we know it contains blue straggler stars (Shara et al. 1998, Clementini et al. in prep.). It is clearly visible that the BSS candidates are associated with the cluster rather than the field population. For Lindsay 1, Kron 3, and NGC 339, the BSS candidates are not as clearly concentrated in the cluster center and are rather younger main-sequence objects of the SMC field.

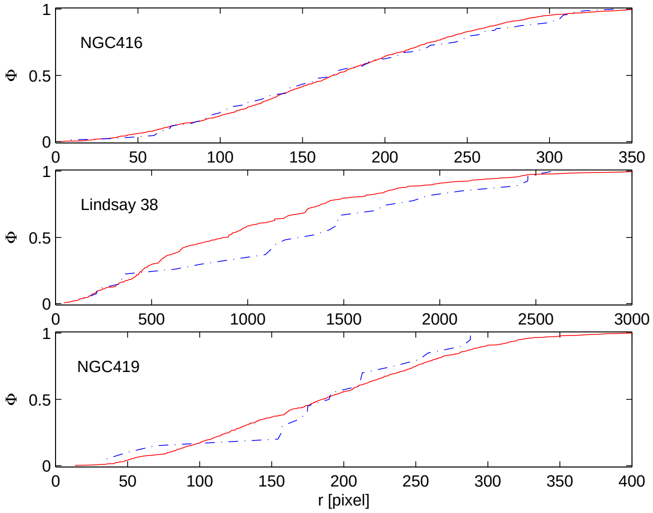

Fig. 17.— Cumulative radial distributions of blue straggler candidates with projected radius for the clusters NGC 416, Lindsay 38, and NGC 419. The solid line represents the 'cluster sample' including the SGB, RGB, and red clump. The dashed line represents the stars found in the BSS region. In Lindsay 38 and NGC 419, the BSS candidates are not significantly concentrated in the cluster center and are likely regular main-sequence stars. The distributions of NGC 416 and NGC 419 are obtained using the HRC sample. In NGC 416 there is indication for centrally concentrated BSS candidates.

The cumulative radial distributions of the selected stars for all clusters can be seen in Figures 16, and 17. The dashed lines show the cumulative distributions for our BSS candidate samples, and the solid lines show the cumulative distributions of the cluster sample for comparison, including the SGB, the lower RGB, and the red clump.

TABLE 3
BSS CANDIDATES

Cluster	Number of BSS candidates [a]
Lindsay 1	110
Kron 3	229
NGC 339	616
NGC 416	91
Lindsay 38	23
NGC 419	8

[a] Number of BSS candidates after removal of stars possibly affected by blends

Each BSS candidate was examined by eye on the image and stars with hints of being affected by blends were eliminated from the catalog (see Table 3). The cumulative distributions of the remaining stars are normalized to our BSS candidate sample. The first panel of Figure 16 shows the cumulative distributions of NGC 121, of which we know that it contains BSSs (Shara et al. 1998, Clementini et al. in preparation). The BSS candidates are evidently more centrally concentrated than the stars from the cluster sample.

In Lindsay 1, Kron 3, NGC 339, Lindsay 38, and NGC419 the blue stars lying above the cluster MSTOs do not show any obvious concentration toward the cluster centers and are fairly evenly distributed across our images. This supports the interpretation that they are not BSS canditates belonging to these clusters, but instead part of the younger MS of the SMC field star population. We have used the Kolmogorov-Smirnov (KS) test to search for statistical differences between the cumulative projected radial distributions. The KS probabilities that BSS candidates and cluster sample stars are extracted from the same parent population are 17% (Lindsay 1), 0% (Kron 3), 0% (NGC 339), 4% (Lindsay 38), and 25% (NGC 419). For NGC 416 and NGC 419, the radial distributions are only shown for the HRC data. Because BSSs are assumed to be located in the cluster center, and the field stars are already overdense in the BSS candidate region on the HRC CMD, the analysis of the HRC data instead of the entire sample is justified. Even though we know that NGC 121 contains BSSs and the radial distribution shows a concentration of the BSS candidates towards the cluster center, the KS-Test gives a probability of 16% that the two samples are from the same distribution.

Within the center region of NGC 416 covered by the HRC data, we find an indication for centrally concentrated BSS candidates. The dashed line (BSS candidate sample) almost lies on top of the solid line (cluster sample). The cluster location is close to the SMC main body, hence some of the BSS candidates are likely field MS stars of the SMC. We will discuss the SMC field stellar population in greater detail in a separate paper. The KS probability for NGC 416 is 85%.

5. CLUSTER AGES

Age determinations of star clusters using isochrones depend crucially on the interstellar extinction, distance and metallicity of the cluster, as well as on the chosen isochrone models. We used spectroscopic metallicities (Da Costa & Hatzidimitriou 1998; Kayser et al. 2006, 2007, Kayser et al. 2008, in preparation) in order to eliminate metallicity as a free parameter when fitting isochrone models. The distance and the extinction were treated as free parameters. The mean SMC distance modulus is assumed to be $(m-M)_0 = 18.88 \pm 0.1$ mag (60 kpc) (e.g., Storm et al. 2004). Due to the large depth extension of the SMC and thus an expected wide spread in the cluster distances we adjusted the distance modulus for each star cluster to produce the best isochrone fits to our CMD data.

TABLE 4
RIDGELINE OF LINDSAY 1

$m_{555} - m_{814}$	m_{555}
1.3230	27.1000
1.1720	26.5000
1.0320	25.9000
0.9090	25.3000
0.7950	24.7000

[a] Table 4 is presented in its entirety in the electronic edition of the Astronomical Journal. A portion of the ridgeline of Lindsay 1 is shown here.

As mentioned before, we visually estimated the location of the cluster center on the image and selected all stars within an individually defined radius on the WFC data, except for NGC 416 and NGC 419 for which we used the HRC data. The center samples were used to fit the fiducial ridgelines for easier comparison to the isochrones.

In order to fit ridgelines, we separated the cluster sample CMDs into three sections: the MS, the SGB and the RGB. On the MS we determined the mode of the color distribution in magnitude bins of 0.3 mag width. For the SGB, we performed a linear least squares fit of a polynomial of 5th order to a Hess diagram of this region in the CMD. Finally, the RGB was fit by a third-order polynomial of the mean color, again in magnitude bins with a size of 0.3 mag each. The resulting ridgelines are shown as cyan lines in our CMDs and will be made available electronically (see Table 4 for an illustrative excerpt).

We fitted our m_{555} vs m_{555}-m_{814} CMDs with three different isochrone models: Padova isochrones (L. Girardi 2006, private communication, Girardi et al. 2000)[10], Teramo isochrones (Pietrinferni et al. 2004) and Dartmouth isochrones (Dotter et al. 2007), all with scaled solar abundances ([α/Fe]=0.0). The Padova isochrone grid has an age resolution of log(t)= 0.01, the Teramo isochrone grid of 0.1 Myr and the Dartmouth isochrone grid of 0.5 Gyr. The Padova isochrones model the AGB and its tip, which is ∼1 mag brighter than the tip of the RGB. The Teramo isochrones include the RGB, HB and the lower AGB. The Dartmouth isochrones terminate at the He flash, because they do not have the HB and the AGB sequence calculated. All sets of isochrones are available in the standard ACS color system.

We fitted a large number of isochrones using different combinations of reddening, age and distance. For each set of models, we selected by trial and error the isochrone that best matched the observed data.

---

[10] http://pleiadi.pd.astro.it/isoc_photsys.02/isoc_acs_wfc/index.html

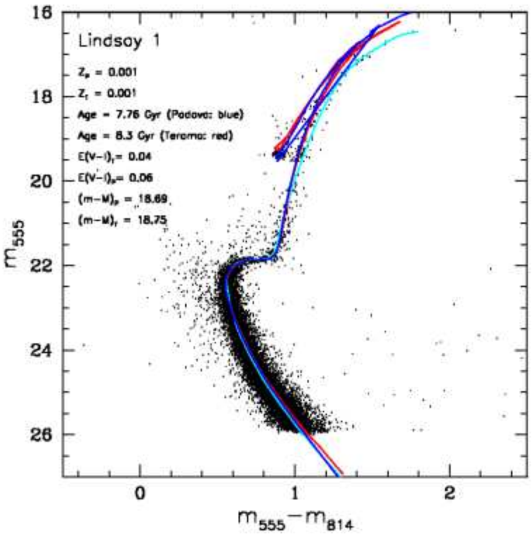

FIG. 18.— The CMD of Lindsay 1 with the best-fitting isochrones of two different models: The blue solid line shows the best-fitting Padova (L.Girardi, 2006, private communication, Girardi et al. 2000) isochrone that is closest to the spectroscopically measured metallicity of the cluster. The red solid line is the best-fitting Teramo (Pietrinferni et al. 2004) isochrone approximating the known metallicity. The cyan solid line is our fiducial ridgeline. The fitting parameters are listed in the plot legend.

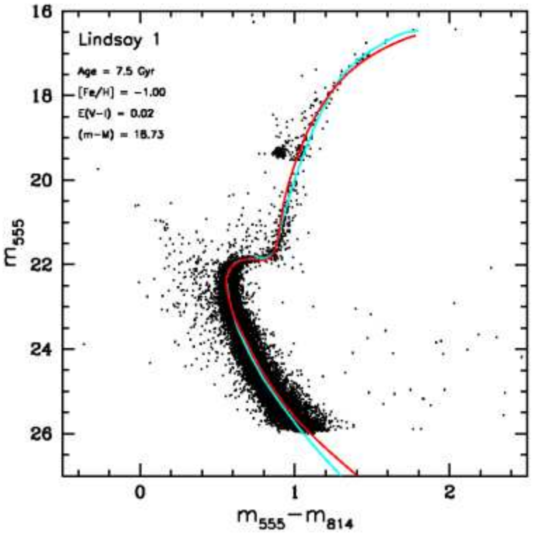

FIG. 19.— The Lindsay 1 CMD with the best-fitting Dartmouth (Dotter et al. 2007) isochrones overplotted in red. As before, the cyan line represents our fiducial for Lindsay 1. The fit parameters are listed in the plot.

5.1. *Age of Lindsay 1*

We adopted the metallicity of [Fe/H] = -1.14±0.10 from Da Costa & Hatzidimitriou (1998) in the scale of Zinn & West (1984) (ZW84). This metallicity corresponds most closely to Z = 0.001 in both the Padova and the Teramo models. Our best-fit age using Padova isochrones is 7.76 Gyr with $(m-M)_0$ = 18.69 mag and E_{V-I} = 0.06. The best fitting Teramo isochrone yields an age of t = 8.3 Gyr, $(m-M)_0$ = 18.75 mag, and E_{V-I} = 0.04 (see Fig. 18).

On the MS, the Padova isochrone is slightly offset to the red by about ∼0.1 mag in color, while the Teramo isochrone is slightly offset by about ∼0.02 mag in color.

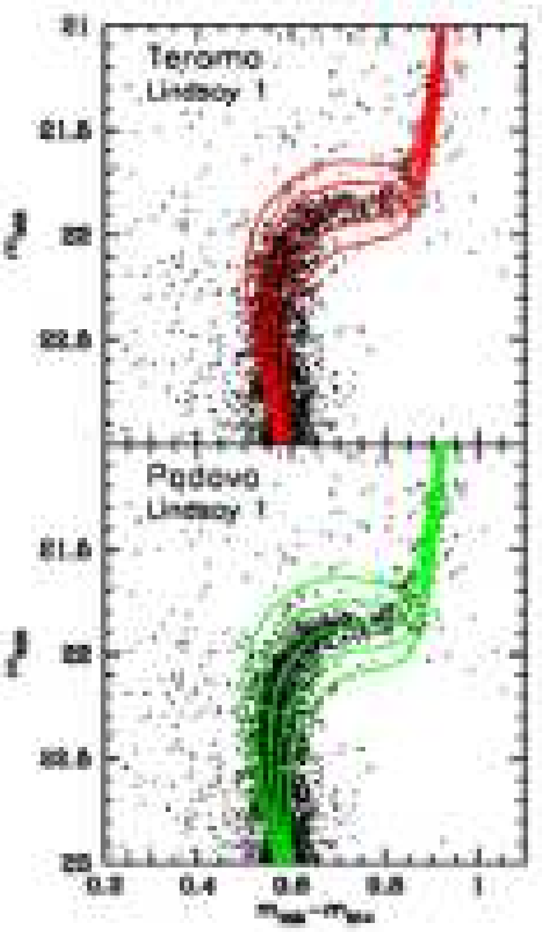

FIG. 20.— The CMD of Lindsay 1 after zooming in on the region of the main-sequence turnoff, subgiant branch, and lower red giant branch. In the upper panel, we show Teramo isochrones as solid lines, covering an age range of 6.8, 7.5, 8.2, 9 and 10 Gyr. In the lower panel we show the same plot for Padova isochrones in the available age steps of 6.16, 6.92, 7.76, 8.7, and 9.77 Gyr. All other parameters are the same as in Figs. 18 and 19.

Between $22 \lesssim m_{555} \lesssim 23$ mag, both the Padova isochrone and the Teramo isochrone are shifted by ∼0.05 mag to the blue with respect to the main ridgeline. Both isochrones provide an excellent approximation to the SGB and to the lower RGB up to about 1 mag below the red clump. At brighter magnitudes, the two isochrones deviate increasingly to the blue of the observed upper RGB. Here the Padova isochrones show the strongest difference, deviating by approximately 0.24 mag in color from the observed tip of the RGB. The Teramo isochrone is too blue by about 0.13 mag at the magnitude of the tip of the RGB.

The best fit using the Dartmouth isochrones is obtained with 7.5 Gyr, $(m-M)_0$ = 18.73 mag and E_{V-I} = 0.02 for an isochrone corresponding to a metallicity [Fe/H] = -1.00 (Fig. 19). As for the Padova and the Teramo isochrones, on the MS the isochrone is ∼0.02 mag offset to the red. The SGB is fitted to a very well and the deviation on the RGB is much smaller than for the other two isochrone models. On the upper RGB, the isochrone is increasingly offset to the red relative to the fiducial ridgeline. The derived reddening by the Dartmouth isochrones agrees best with the extinction A_V = 0.1 from the Schlegel et al. (1998) maps (E_{V-I} =

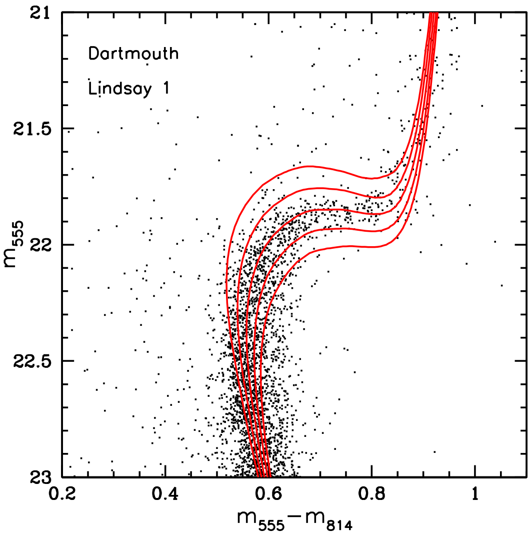

Fig. 21.— Same as Fig. 20, but for the Dartmouth isochrones with ages of 6.5, 7, 7.5, 8 and 8.5 Gyr.

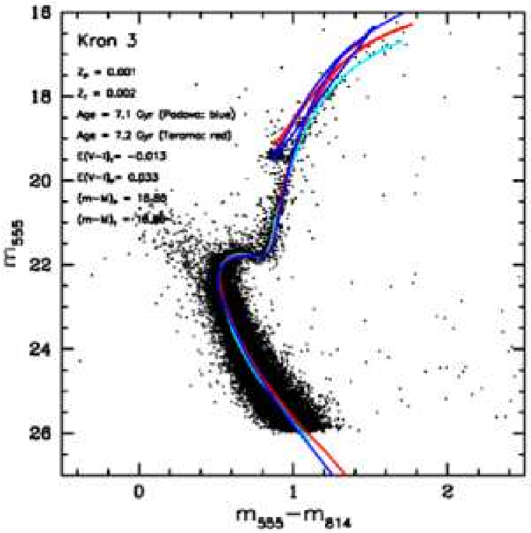

Fig. 22.— The CMD of Kron 3 with the best-fitting isochrones of two different models: The blue solid line shows the best-fitting Padova isochrone that is closest to the spectroscopically measured metallicity of the cluster. The red solid line is the best-fitting Teramo isochrone approximating the known metallicity. The cyan solid line is our fiducial ridgeline. The fit parameters are listed in the plot legend.

0.024 mag). The reddening law of Dean et al. (1978) is assumed.

In the Figures 20 and 21 we show a range of isochrones for the three sets of stellar evolution models in order to illustrate the age uncertainty in a given model. The best fit isochrone is always displayed along with two younger and two older isochrones. Due to the high quality of the fit of the central isochrone in the region of the upper MS, SGB, and lower RGB in all models and the larger deviations of the adjacent isochrones, we estimate that the resultant age uncertainty is of the order of approximately ± 0.7 Gyr for the Teramo and Padova isochrones and ± 0.5 Gyr for the Dartmouth isochrones.

5.2. *Age of Kron 3*

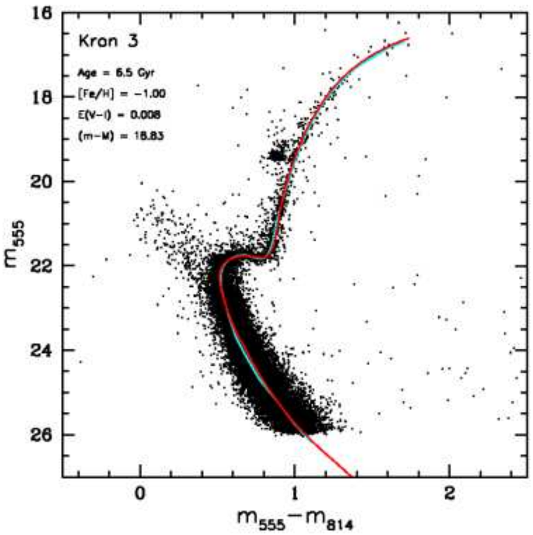

Fig. 23.— The Kron 3 CMD with the best-fitting Dartmouth isochrones overplotted in red. As before, the cyan line represents our fiducial for Kron 3. The fit parameters are listed in the plot.

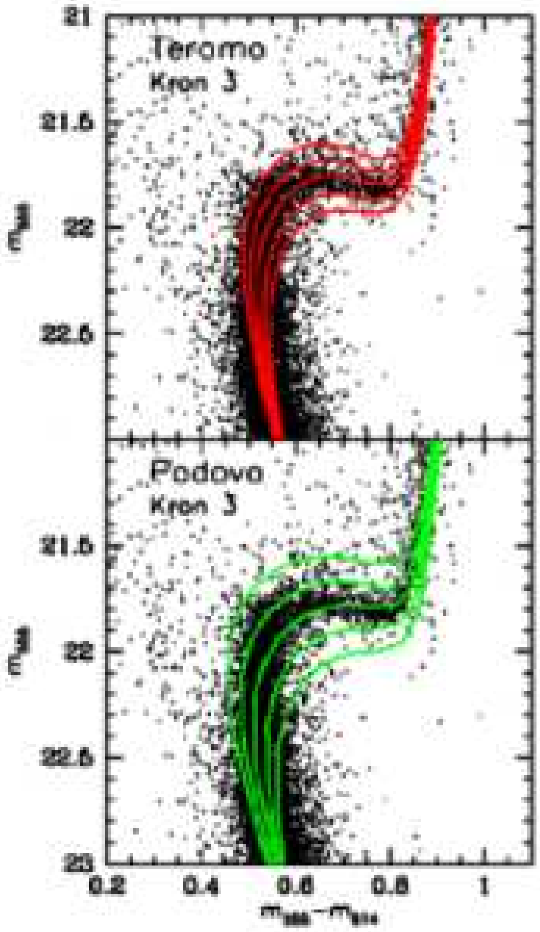

Fig. 24.— The CMD of Kron 3 after zooming in on the region of the main-sequence turnoff, subgiant branch, and lower red giant branch. In the upper panel, we show Teramo isochrones as solid lines, covering an age range of 5.2, 6.1, 7, 7.8, and 8.4 Gyr. In the lower panel we show the same plot for Padova isochrones in the available age steps of 5.6, 6.3, 7.1, 7.9, and 8.9 Gyr. All other parameters are the same as in Figs. 22 and 23.

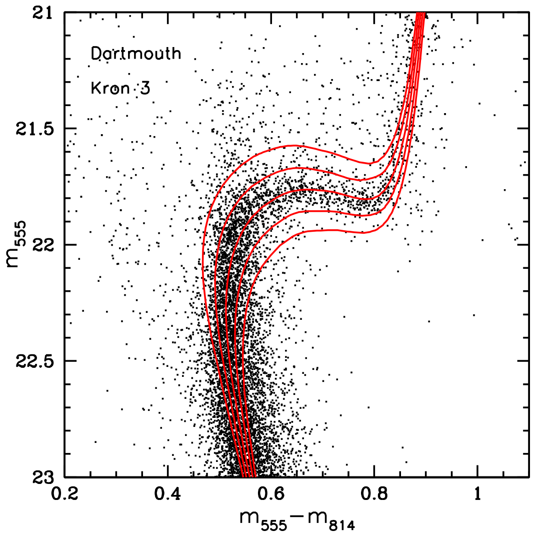

FIG. 25.— Same as Fig. 24, but for the Dartmouth isochrones with ages of 5.5, 6, 6.5, 7, and 7.5 Gyr.

We adopted the spectroscopic metallicity derived by Da Costa & Hatzidimitriou (1998) of [Fe/H] = -1.08 ± 0.12. This metallicity corresponds most closely to Z=0.001 in the Padova models, Z=0.002 in the Teramo models and [Fe/H] = -1.00 in the Dartmouth models. The best-fit age using the Padova isochrones was found to be 7.1 Gyr, $(m-M)_0 = 18.80$ mag and $E_{V-I} = 0.033$. The best fit for the Teramo isochrones is obtained with t = 7.2 Gyr, $(m-M)_0 = 18.80$ mag and E_{V-I} = -0.013 (Fig. 22). No reasonable fit with a zero or positive reddening value was obtained.

On the MS, both isochrones are slightly offset to the red by about ∼0.02 (Teramo) and ∼0.01 (Padova) in color. The Teramo isochrone traces the SGB and the lower RGB to a high accuracy. Only at the faint end of the SGB the isochrone is about ∼0.02 mag brighter than our fiducial ridgeline. The isochrone deviates increasingly to the blue of the observed upper RGB, but fits the color of the RGB tip very well with a small deviation of about 0.02 mag. The base of the red clump, however, is ∼0.4 mag too bright. The Padova isochrone lies ∼0.1 mag below our observed SGB and is ∼0.02 mag offset in color on the lower RGB. The isochrone continues further to the blue on the upper RGB as seen for the Teramo isochrone. The Padova isochrone shows the strongest difference at the RGB tip, deviating by approximately 0.22 mag in color from the observed tip of the RGB. The base of the red clump is fitted very well.

The Dartmouth isochrone model provided by Dotter et al. (2007) yields the best fit to the CMD (Fig. 23). The best-fit isochrone has the parameters t = 6.5 Gyr, $(m-M)_0 = 18.83$ and $E_{V-I} = 0.008$. All the major features of the CMD are very well reproduced, including the upper RGB where the isochrone is offset slightly to the blue relative to the fiducial ridgeline. This offset is no more than 0.02 mag on average along the entire upper RGB. Even the slope of the RGB is very well reproduced along its entire extent. The derived reddening for Padova isochrones agrees best with the extinction $A_V = 0.09$ from the Schlegel et al. (1998) maps ($E_{V-I} = 0.024$ mag).

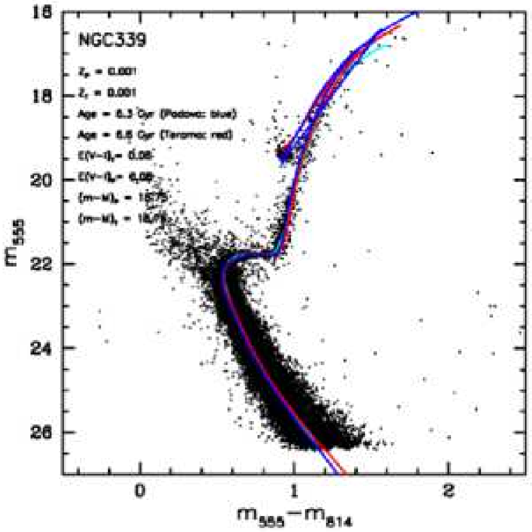

FIG. 26.— The CMD of NGC 339 with the best-fitting isochrones of two different models: The blue solid line shows the best-fitting Padova isochrone that is closest to the spectroscopically measured metallicity of the cluster. The red solid line is the best-fitting Teramo isochrone approximating the known metallicity. The cyan solid line is our fiducial ridgeline. The fit parameters are listed in the plot legend.

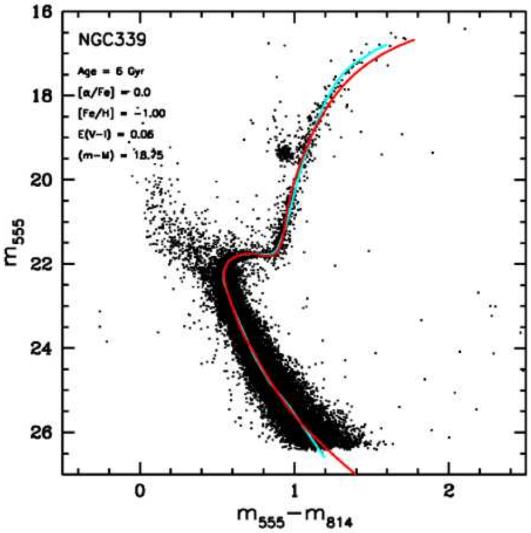

FIG. 27.— The NGC 339 CMD with the best-fitting Dartmouth isochrones overplotted in red. As before, the cyan line represents our fiducial for NGC 339. The fit parameters are listed in the plot.

In Figures 24 and 25 we display our "best" isochrone along with two older and two younger ones for each model. Here the deviations of these isochrone models from the observed upper MS and SGB are very clearly visible. We estimate the resultant age uncertainty in order of approximately ± 0.5 Gyr for the Teramo and Dartmouth isochrones and ± 0.7 Gyr for the Padova isochrones.

5.3. *Age of NGC 339*

We adopted a spectroscopic metallicity of [Fe/H] = -1.12 ± 0.10 from Da Costa & Hatzidimitriou (1998), which made us use isochrones with Z = 0.001 for both the Teramo and the Padova models. The best age fit using the Teramo isochrone is found with the parameters t = 6.6 Gyr, $(m-M)_0 = 18.75$ mag and $E_{V-I} = 0.08$.

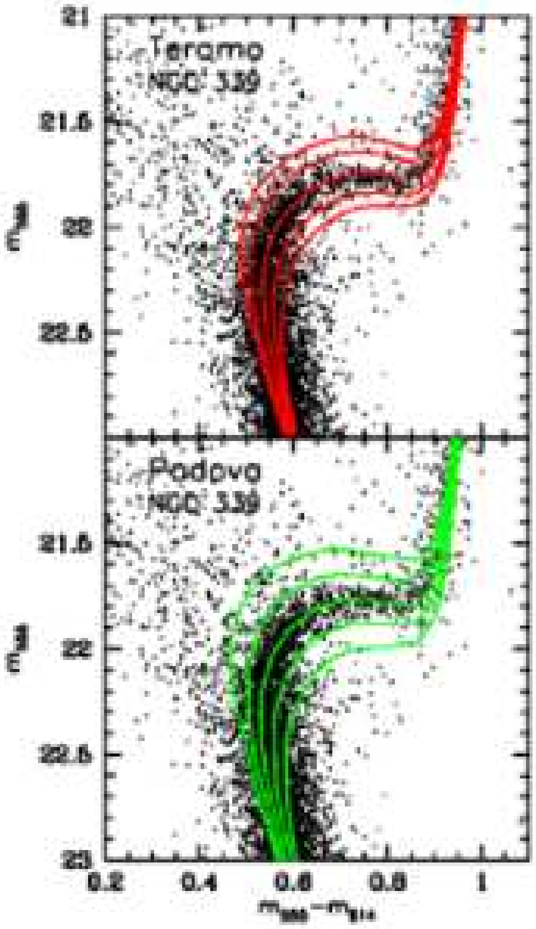

Fig. 28.— The CMD of NGC 339 after zooming in on the region of the main-sequence turnoff, subgiant branch, and lower red giant branch. In the upper panel, we show Teramo isochrones as solid lines, covering an age range of 5.6, 6, 6.6, 7.2, and 7.7 Gyr. In the lower panel we show the same plot for Padova isochrones in the available age steps of 5, 5.6, 6.3, 7, and 7.9 Gyr. All other parameters are the same as in Figs. 26 and 27.

Our best fitting Padova isochrone yields an age of t = 6.3 Gyr with $(m-M)_0 = 18.75$ mag and $E_{V-I} = 0.08$.

Both isochrones provide an excellent approximation to all features of the CMD (Fig. 26), the MS, the SGB and even the upper RGB, where the isochrones are only slightly offset to the blue relative to the fiducial ridgeline. These offsets are no more than 0.01 mag (Teramo) and 0.03 mag (Padova) in color on average along the entire upper RGB. Also the slope of the RGB is very well reproduced along its entire extent. At the RGB tip, the Padova isochrone deviates by approximately 0.15 mag in color to the red from the observed RGB tip, while the Teramo isochrone match the observed color and luminosity of the tip better, deviating ~ 0.10 mag in color to the red. The Teramo isochrone shows a magnitude for the base of the red clump that is about 0.2 brighter than the observed one. The Padova isochrone indicates a magnitude for the base of the red clump that is 0.2 mag too faint.

Figure 27 shows the best-fit isochrone for the Dartmouth model. The best fit is obtained with an age of t = 6 Gyr and the parameters $(m-M)_0 = 18.75$ mag and $E_{V-I} = 0.06$. The Dartmouth isochrone traces the ridgeline on the MS, the SGB and the lower RGB to a very well. On the lower RGB, the isochrone is offset to the blue by $\sim$0.03 mag, while on the upper RGB it is $\sim$0.05 mag too red. The derived reddening for Dartmouth isochrones agrees best with the extinction $A_V = 0.15$ from the Schlegel et al. (1998) maps ($E_{V-I} = 0.04$ mag).

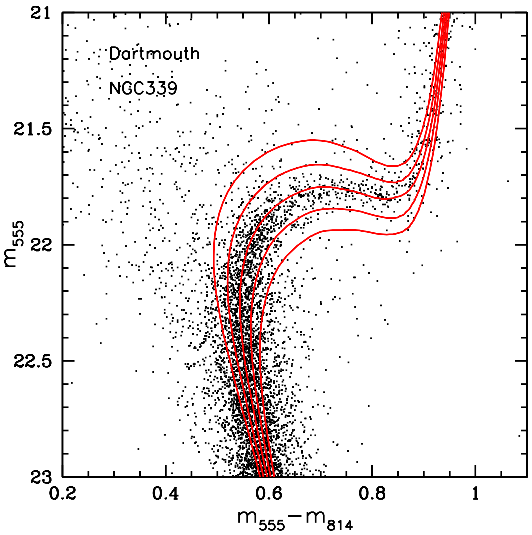

Fig. 29.— Same as Fig. 28, but for the Dartmouth isochrones with ages of 5, 5.5, 6, 6.5, and 7 Gyr.

In Figures 28 and 29 we show a range of isochrones for each model to illustrate the age uncertainty. We always display our "best" fit isochrone along with two older and two younger ones. Considering the excellent fit of all age-sensitive features of the CMD by all three stellar evolution models, we estimate the resultant age uncertainty to be approximately ±0.5 Gyr for all three models.

5.4. *Age of NGC 416*

The latest spectroscopic metallicity measurement was performed by Kayser et al. (2008, in preparation) and yields a metallicity $[Fe/H]_{CG97} = -0.87 \pm 0.06$ in the scale of Carretta & Gratton (1997) (CG97) . We transform this metallicity to the ZW84 scale using the transformation given by Carretta & Gratton (1997), and obtain a metallicity of $[Fe/H]_{ZW84} = -1.00$. This metallicity corresponds most closely to Z = 0.002 for both the Teramo and the Padova models. In Figure 30, the CMD with the overplotted Teramo and Padova isochrones is shown. The best fit for the Teramo isochrones is obtained with t = 6.0 Gyr, $(m-M)_0 = 18.88$ mag and $E_{V-I} = 0.105$, while the Padova isochrones provide t = 6.6 Gyr, $(m-M)_0 = 18.76$ mag and $E_{V-I} = 0.10$. The relatively high reddening value is due to the location of the cluster close to the SMC main body (see Fig. 1).

On the MS, both the Teramo isochrone and the Padova isochrone are offset to the blue by about $\sim$0.01 mag. While the Teramo isochrone fits the MSTO rather nicely, the Padova isochrone is $\sim$0.05 mag too blue. At the blue end of the SGB, both isochrones are slightly too faint. The Teramo isochrone fits the red part of the SGB and the entire RGB almost perfectly up to about 0.5 magnitudes below the RGB tip (see Fig. 30). The Padova isochrone fits the red end of the SGB almost perfectly, but deviates increasingly to the blue on the RGB with respect to our fiducial ridgeline. The isochrone shows a

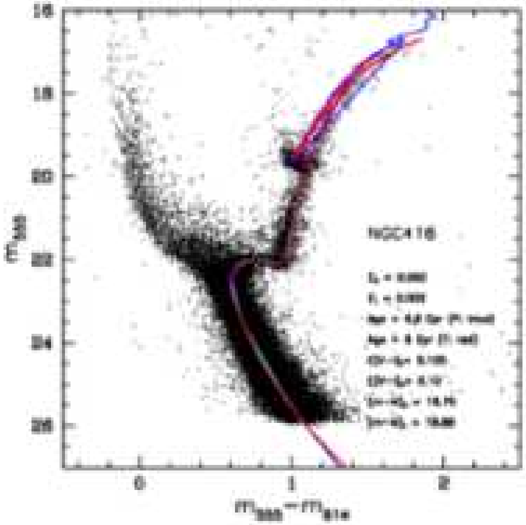

FIG. 30.— The CMD of NGC 416 with the best-fitting isochrones of two different models: The blue solid line shows the best-fitting Padova (L.Girardi, 2006, in preparation) isochrone that is closest to the spectroscopically measured metallicity of the cluster. The red solid line is the best-fitting Teramo (Pietrinferni et al. 2004) isochrone approximating the known metallicity. The cyan solid line is our fiducial ridgeline. The fit parameters are listed in the plot legend.

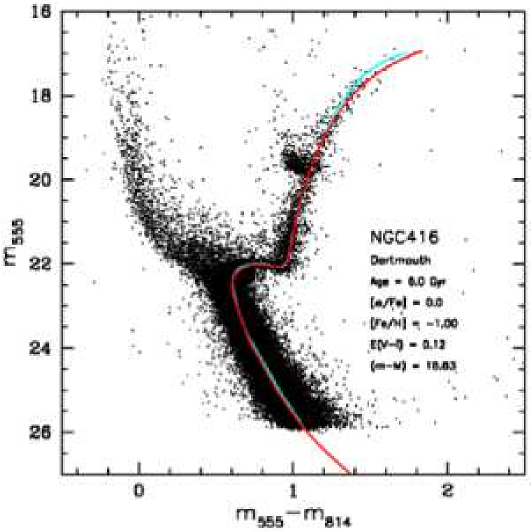

FIG. 31.— The NGC 416 CMD with the best-fitting Dartmouth (Dotter et al. 2007) isochrones overplotted in red. As before, the cyan line represents our fiducial for NGC 416. The fit parameters are listed in the plot.

magnitude for the base of the red clump that is about 0.1 mag brighter than the observed one. The Teramo isochrone indicates a magnitude for the base of the red clump that is 0.25 mag too bright.

In Figure 31 the best fitting isochrone for the Dartmouth models (Dotter et al. 2007) is displayed with t = 6 Gyr, $(m-M)_0 = 18.83$ mag and $E_{V-I} = 0.12$. We adopted the isochrone set with a metallicity of [Fe/H] = −1.0. All age-sensitive features of the CMD are well reproduced. On the upper RGB, the isochrone is increasingly offset to the blue relative to the fiducial ridgeline with 0.03 mag in color being the strongest difference. Our derived reddenings agree with the extinction A_V

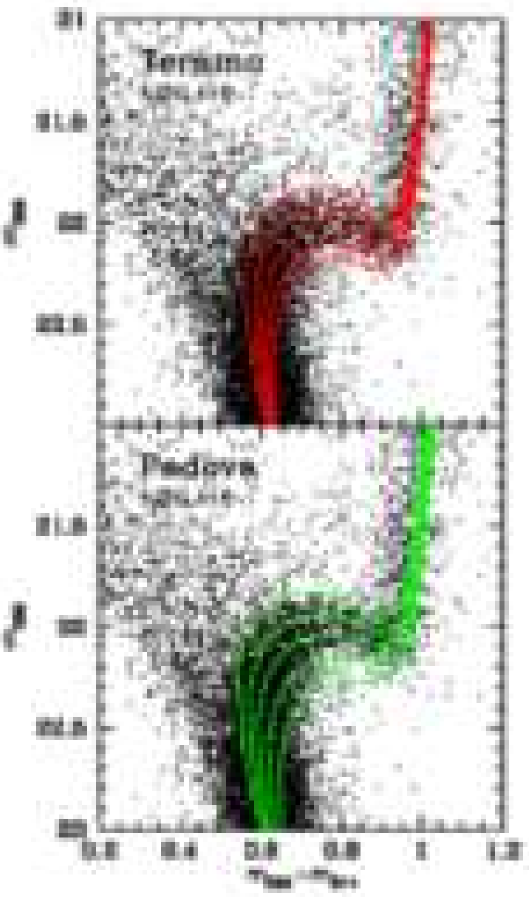

FIG. 32.— The CMD of NGC 416 after zooming in on the region of the main-sequence turnoff, subgiant branch, and lower red giant branch. In the upper panel, we show Teramo isochrones as solid lines, covering an age range of 5, 5.5, 6, 6.5, and 7 Gyr. In the lower panel we show the same plot for Padova isochrones in the available age steps of 5.4, 6.0, 6.6, 7.4, and 8.3 Gyr. All other parameters are the same as in Figs. 30 and 31.

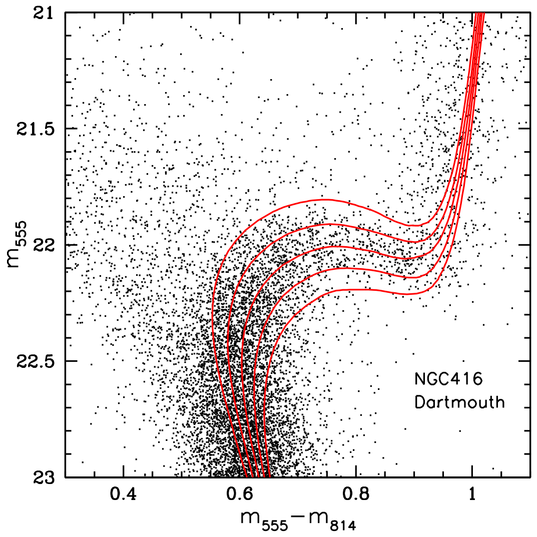

FIG. 33.— Same as Fig. 32, but for the Dartmouth isochrones with ages of 5, 5.5, 6, 6.5, and 7 Gyr.

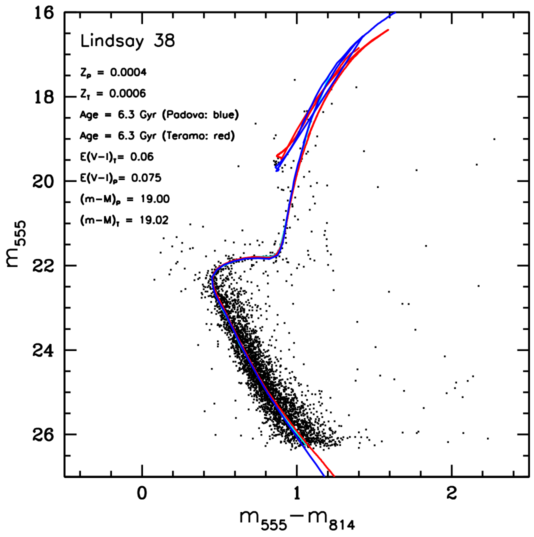

Fig. 34.— The CMD of Lindsay 38 with the best-fitting isochrones of two different models: The blue solid line shows the best-fitting Padova isochrone that is closest to the spectroscopically measured metallicity of the cluster. The red solid line is the best-fitting Teramo isochrone approximating the known metallicity. The cyan solid line is our fiducial ridgeline. The fit parameters are listed in the plot legend.

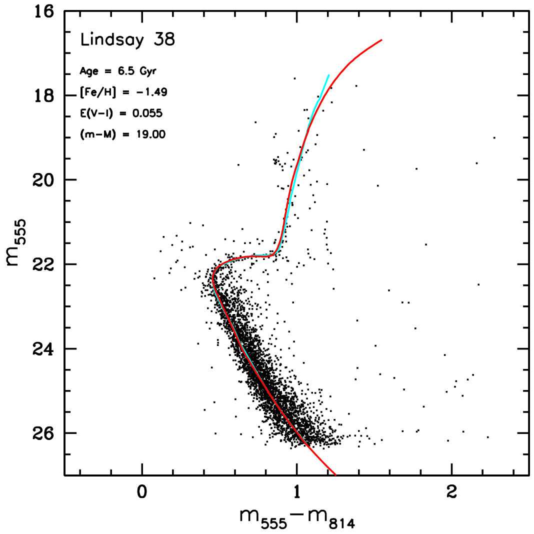

Fig. 35.— The Lindsay 38 CMD with the best-fitting Dartmouth isochrones overplotted in red. As before, the cyan line represents our fiducial for Lindsay 38. The fit parameters are listed in the plot.

= 0.32 from the Schlegel et al. (1998) maps (E_{V-I} = 0.1 mag).

In Figures 32 and 33 a range of five isochrones is displayed for each isochrone model. Even though the approximation of all features that are important for the age determination important features is close, we estimate the age uncertainty to be ∼0.8 Gyr. It is possible that the broad width of the RGB suggests a spread in metallicity and therefore in age, which we have to take into account. The main reason for the broadening of the RGB, however, are SMC field stars.

5.5. *Age of Lindsay 38*

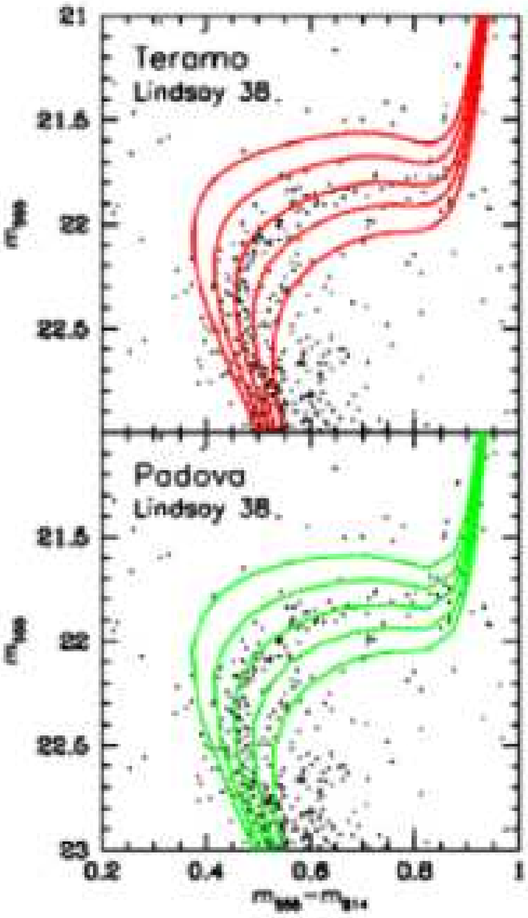

Fig. 36.— The CMD of Lindsay 38 after zooming in on the region of the main-sequence turnoff, subgiant branch, and lower red giant branch. In the upper panel, we show Teramo isochrones as solid lines, covering an age range of 5, 5.6, 6.3, 7, and 8 Gyr. In the lower panel we show the same plot for Padova isochrones in the available age steps of 5, 5.6, 6.3, 7.1, and 7.9 Gyr. All other parameters are the same as in Figs. 34 and 35.

The latest measured spectroscopic metallicity provided by Kayser et al. (2006, 2007, 2008 in prep.) is $[Fe/H]_{CG97} = -1.35 \pm 0.10$, which we transformed to $[Fe/H]_{ZW84} = -1.59$ (Carretta & Gratton 1997). This metallicity is in excellent agreement with the photometric metallicity found by Piatti et al. (2001). We used isochrones of Z = 0.0004 in the Padova models, Z = 0.0006 in the Teramo models and [Fe/H] = -1.49 in the Dartmouth models. The best-fit age using the Teramo isochrone is t = 6.3 Gyr with $(m-M)_0 = 19.02$ mag and $E_{V-I} = 0.06$. The best fitting Padova isochrone yields an age of t = 6.3 Gyr, $(m-M)_0 = 19.00$ and $E_{V-I} = 0.075$ (Fig. 34). Surprisingly, Lindsay 38 is the only cluster for which we found a high quality fit using α-enhanced Dartmouth isochrones ([α/Fe] = +0.20), which yield an age of 6 Gyr using the same fitting parameters.

All features of the CMD are traced very well by both the Teramo and the Padova isochrones. At the faint end of the MS, the Teramo isochrone continues further to the red than the Padova isochrone and our derived ridgeline; however, this only becomes more apparent at magnitudes of m_{555} = 25.5 mag and below. The MS, the SGB and the lower RGB are very well reproduced. The upper part of the RGB is too sparse for the fit of

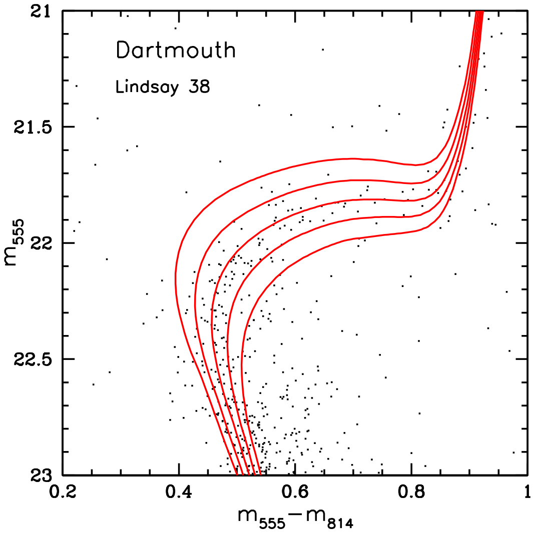

FIG. 37.— Same as Fig. 36, but for the Dartmouth isochrones with ages of 5.5, 6, 6.5, 7, and 7.5 Gyr.

a ridgeline. Therefore, a statement about the quality of the theoretical fiducials cannot be made. The base of the red clump for the Padova isochrone is about 0.2 mag too faint, while for the Teramo isochrone it is about 0.4 mag too bright.

In Figure 35 the best-fit age provided by the Dartmouth isochrone (Dotter et al. 2007) is shown with t = 6.5 Gyr, $(m-M)_0 = 18.94$ mag and $E_{V-I} = 0.05$ (red line in Fig. 35). The MS and the SGB are very well reproduced. The lower RGB is slightly offset by about 0.02 on average along the entire RGB. The isochrone deviates increasingly to the red starting at 1.5 mag above the red clump. The reddening value found using isochrones is too high compared with the extinction taken from the Schlegel et al. (1998) maps ($A_V = 0.05$, $E_{V-I} = 0.016$ mag).

In Figures 36 and 37 we show a selection of isochrones to estimate the age uncertainty. For each isochrone model two older and two younger isochrones are shown along with the "best" one. We estimate the age uncertainty to be ± 0.5 Gyr for all of the three isochrone models.

5.6. *Age of NGC 419*

The latest spectroscopic metallicity measurement was performed by Kayser et al. (2008, in preparation) and yields a metallicity $[Fe/H]_{CG97} = -0.71 \pm 0.12$ in the CG97 scale. We transform this metallicity to the ZW84 scale using the transformation given by Carretta & Gratton (1997), and obtain a metallicity of $[Fe/H]_{ZW84} = -0.67$. This metallicity corresponds most closely to Z = 0.004 (Padova and Teramo) and $[Fe/H] = -0.5$ (Dartmouth). The best fit for the Padova isochrones provides t = 1.25 Gyr with $(m-M)_0 = 18.75$ mag and $E_{V-I} = 0.12$ (see Fig. 38). The best-fit age using the Dartmouth isochrones is t = 1.5 Gyr with $(m-M)_0 = 18.60$ mag and $E_{V-I} = 0.07$. The Teramo model has problems with fitting all cluster features simultaneously (see Fig. 39). The best-fitting age is t = 1 Gyr with $(m-M)_0 = 18.94$ mag and $E_{V-I} = 0.11$. Note that it is not obvious where the exact location of NGC419's MSTO is.

As for NGC 416, we find a relatively high reddening parameter due to the cluster location close to the SMC main body, where also a lot of crowding is expected. The Padova isochrone fits the MS and the SGB very well, while the lower RGB is offset by ~0.05 mag in color, and its slope is not fitted at all. The isochrone does not fit the red clump, lies ~0.02 mag to the red and is ~0.6 mag too faint.

In Figure 41 we show Padova isochrones superimposed on the NGC 419 region. These are isochrones of 1.25, 1.4, and 1.6 Gyr. Because the exact location of the MSTO of the cluster is uncertain, we do not give a single age for NGC 419. Instead, we determine an age range of 1.2-1.6 Gyr.

In Figure 39 we can clearly see the inability of the Teramo isochrones to fit all cluster features simultaneously. The best-fitting Teramo isochrone (1 Gyr) deviates increasingly to the blue along the MS. At the MSTO the isochrone is about 0.15 mag offset to the blue. The RGB turn-off is ~0.2 mag too faint and the isochrone deviates again increasingly to the blue on the RGB.

The two youngest available Dartmouth isochrones have an age of 1 and 1.5 Gyr (Fig. 40). The age of NGC 419 lies between these two isochrones. This might be the reason why the best-fitting Dartmouth isochrone does not provide a very good fit. The isochrone fits the RGB slope very well, but is ~0.04 mag offset to the blue at the RGB turn-off. The isochrone is ~0.25 mag too bright at the blue end of the SGB, and on the MS, the isochrone is slightly offset by about ~0.02 mag to the red. In Figure 42 we show the isochrones of 1 and 2 Gyr for comparison, which are obviously either too old or too young for NGC 419. As for the Padova isochrones, we cannot give a single age for NGC 419 and confirm the age range of 1.2-1.6 Gyr using the Dartmouth isochrones. Our derived reddening using the Dartmouth isochrone agrees with the extinction $A_V = 0.31$ from the Schlegel et al. (1998) maps ($E_{V-I} = 0.08$ mag), while the reddening values found using the Padova and the Teramo isochrones are too high.

Because of the complexity of NGC 419, we will discuss its CMD in more detail in a separate paper.

6. DISTANCES

There are no direct determinations of the cluster distances along the line-of-sight, but it is assumed that the SMC as a depth extent of up to 20 kpc (Mathewson et al. 1988; Hatzidimitriou et al. 1993; Crowl et al. 2001; Lah et al. 2005). We assume that the main body of the SMC has a distance modulus of $(m-M)_0 = 18.88 \pm 0.1$ mag (e.g., Storm et al. 2004).

In addition to the distance estimates that result from our isochrone fits, we can use the apparent magnitudes of the red clump measured in this paper to provide a distance estimate for our clusters. We use the absolute red clump magnitudes $\langle M_V \rangle$ given in Girardi & Salaris (2001), as a function of age and metallicity. These authors provide mean properties of the red clump for metallicities from Z=0.0004 to 0.03, and ages from 0.5 to 12 Gyr, based on the theoretical horizontal branch models of Girardi et al. (2000, see also Girardi & Salaris 2001). We corrected our distance modulus for the interstellar extinction by consulting the Schlegel maps (Schlegel et al. 1998). The adopted parameters and the

TABLE 5
Distance Estimate

Cluster	$V_{HB,RC}$ mag	$\langle M_V \rangle$ mag	$E_{V-I,SM}$ mag	$(m-M)$ mag	Distance kpc
NGC 121	19.71 ± 0.03	0.574	0.024	19.06 ± 0.03	64.9 ± 1.2
Lindsay 1	19.36 ± 0.04	0.509	0.024	18.78 ± 0.04	56.9 ± 1.0
Kron 3	19.46 ± 0.03	0.474	0.024	18.91 ± 0.04	60.6 ± 1.1
NGC 339	19.38 ± 0.08	0.455	0.040	18.80 ± 0.08	57.6 ± 4.1
NGC 416	19.70 ± 0.07	0.474	0.104	18.90 ± 0.07	60.4 ± 1.9
Lindsay 38	19.60 ± 0.05	0.430	0.016	19.12 ± 0.05	66.7 ± 1.6
NGC 419	19.41 ± 0.12	-	0.080	18.50 ± 0.12	50.2 ± 2.6

[a] The values for $V_{HB,RC}$ are taken from this paper and Paper I. The values for $\langle M_V \rangle$ were adopted from Girardi & Salaris (2001). For NGC 121 and Lindsay 38, we chose the model of Z=0.004, for Lindsay 1, Kron 3, NGC 339, and NGC 416 the model of Z=0.001, and for NGC 419 the model of Z=0.004. The reddenings E_{B-V} are taken from the Schlegel maps (Schlegel et al. 1998) and transformed into E_{V-I} by adopting $E_{V-I}/E_{B-V} = 1.25$ from Dean et al. (1978). For NGC 419 not the luminosity of the red clump but the distance modulus found with the Padova isochrones ($(m-M) = 18.75$) was used to determine the distance due to the age and metallicity dependence of the absolute red clump magnitude.

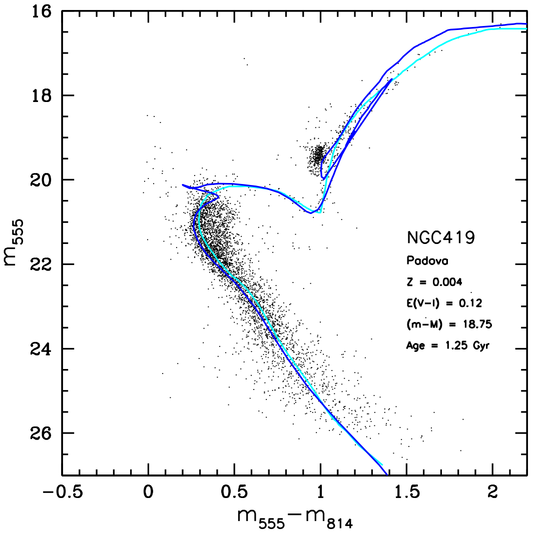

Fig. 38.— The CMD of NGC 419 with the best-fitting isochrone of the Padova model: the blue solid line shows the best-fitting Padova isochrone that is closest to the spectroscopically measured metallicity of the cluster. The distinction of the cluster from the field population is difficult due to the multiple turnoffs and the sparse SGB.

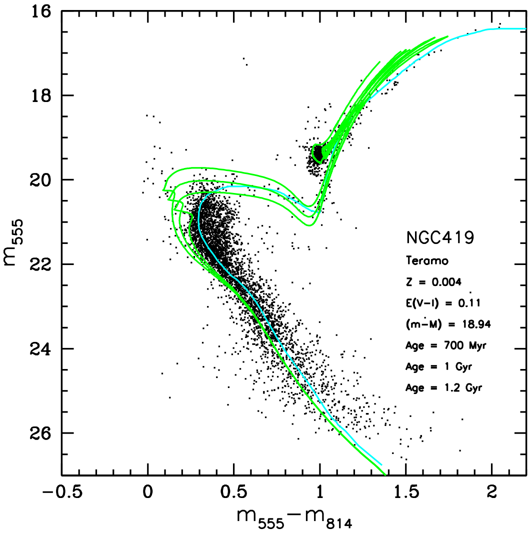

Fig. 39.— The CMD of NGC 419 with the Teramo isochrones overplotted in green. As before, the cyan line represents our fiducial for NGC 419. We show isochrones in the age range of 0.8, 1, 1.2 Gyr. The fit parameters are listed in the plot.

resulting distances are listed in Table 5. Due to the fact that NGC 419 may be a multiple population object and therefore its age and the metallicity are uncertain, we do not use its absolute red clump magnitude for the distance estimate. Instead we apply the distance modulus found using the Padova isochrones (m-M) = 18.75 mag and correct for the extinction.

We find that Lindsay 38 is the most distant cluster of our sample with a distance modulus $(m-M) = 19.12$ mag (∼67 kpc), while NGC 419 is the closest cluster with a distance modulus of $(m-M) = 18.50$ mag (∼50 kpc). NGC 419 thus has a similar distance from us as the LMC, whose distance modulus is 18.50 ± 0.02 mag (e.g., Alves 2004). Taking NGC 419 into account, the closest and farthest cluster in our sample have a distance from each other of ∼17 kpc. Excluding NGC 419, the depth extension of the SMC as derived from our cluster sample is ∼10 kpc. We have to emphasize that the distance of NGC 419 is the most uncertain of our sample due to its complexity.

Crowl et al. (2001) used the same approach and derived distances for 12 clusters, six of which overlap with our sample. Their determined distance values are generally lower then the values we obtained, due to fainter absolute red clump magnitudes, which they adopted from Sarajedini (1999). Crowl et al. (2001) do not have NGC 419 in their sample, but NGC 411, NGC 152, Lindsay 113, NGC 361, Kron 28, and Kron 44. The closest cluster using the reddening values from the Schlegel maps is Kron 28 (45.2 ± 1.7 kpc), and the farthest cluster is NGC 121 (65.4 ± 1.9 kpc). Therefore Kron 28 is ∼3 kpc closer than NGC 419. In Crowl et al.'s sample, the clusters have a maximum distance of 20.2 kpc from one another, which is a higher value than what we have found with our smaller cluster sample.

7. DISCUSSION

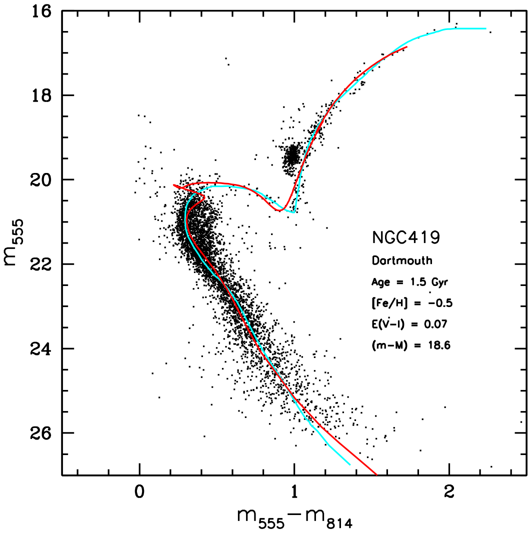

FIG. 40.— The CMD of NGC 419 with the best-fitting Dartmouth isochrone overplotted in red. As before, the cyan line represents our fiducial for NGC 419. The fit parameters are listed in the plot.

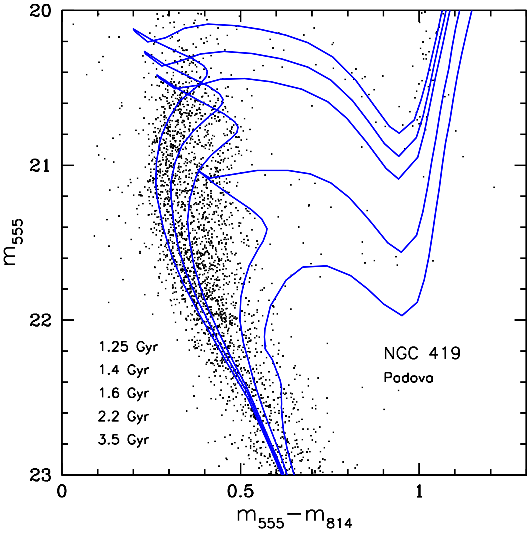

FIG. 41.— The CMD of NGC 419 after zooming in to the region of the MSTO, SGB, and lower RGB. We show Padova isochrones as solid lines to estimate the age of the cluster and field population visible in the CMD. The isochrones cover an age range of 1.25, 1.4, 1.6, 2, and 3.5 Gyr. All other parameters are the same as in Fig. 38.

7.1. *Comparison of our age determination with previous studies*

Previous studies done by several different authors provided ages and metallicities of SMC star clusters using a variety of techniques and telescopes. Therefore, if we combine all published cluster ages, we find a wide range of ages and metallicities for a given cluster, depending on the method used for the determination: Lindsay 1 has an age range from 7.3-10 Gyr (Gascoigne 1966, 1980; Olszewski et al. 1987; Sarajedini et al. 1995; Mighell et al. 1998b; Udalski 1998; Alcaino et al. 2003), Kron 3 from 5-10 Gyr (Gascoigne 1966; Rich et al. 1984; Alcaino et al. 1996; Mighell et al. 1998b; Udalski 1998; Rich et al. 2000), and NGC 339 from 5-7.9 Gyr (Mighell et al. 1998b; Udalski 1998; Rich et al. 2000).

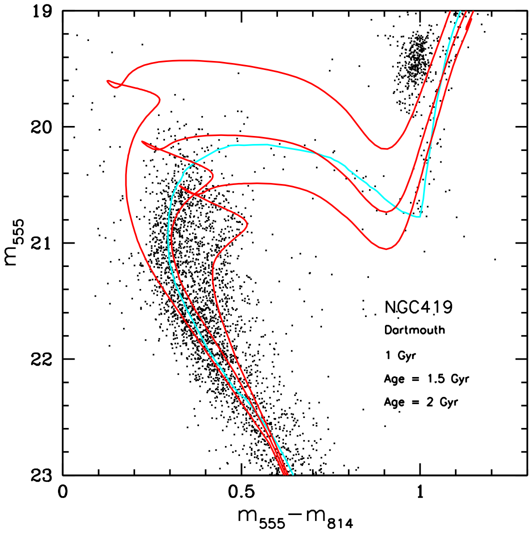

FIG. 42.— Same as Fig. 41, but for the Dartmouth isochrones with ages of 1, 1.5, and 2 Gyr.

No other cluster has such a wide range of different age determinations as NGC 416, reaching from 2.5-11.2 Gyr (Durand et al. 1984; Elson & Fall 1985; Bica et al. 1986; Mighell et al. 1998b; Udalski 1998; Rich et al. 2000). The cluster is located close to the SMC main body where a large interstellar extinction is expected. The separation of field stars from the real cluster members was a major problem in the age determination process, among uncertain values for metallicity, reddening and distance. Using photometry obtained with the Wide Field Planetary Camera 2 (WFPC2) aboard HST, Mighell et al. (1998b) found an absolute age of 6.6±0.5 Gyr for NGC 416, while Rich et al. (2000) derived an age of 7.1 to 11.2 Gyr using the same data set.

The only available CMD of Lindsay 38 is provided by Piatti et al. (2001). The observation was carried out with the Cerro Tololo Inter-American Observatory (CTIO) 0.9 m telescope using the Tektronix 2K # 3 CCD. They presented the first age determination of Lindsay 38 with 6 ± 0.6 Gyr. For NGC 419, the latest CMD was published by Rich et al. (2000) based on WFPC2 data. Udalski (1998) published an age of 3.3 Gyr and Rich et al. (2000) give an age range of $1.0 - 1.8$ Gyr.

For Lindsay 1, Kron 3, NGC 339, NGC 416, and NGC 419, the latest and deepest available CMD was provided with WFPC2 (Mighell et al. 1998b; Rich et al. 2000), while for Lindsay 38 only ground-based data existed.

In Table 6 we compare our ages using the best-fitting Dartmouth isochrones (except NGC 419, for which the Padova isochones provided the best fit) with results published in the most recent studies based on HST/WFPC2 photometry. The data reach ∼2 mag below the turnoff points, while our ACS data have a depth of 3.5 mag below turnoffs. We can see that Mighell et al. (1998b) derived a similar age for Lindsay 1, while for the remaining clusters in the overlapping sample they found younger ages than the ones derived here. Rich et al. (2000), who used the same WFPC2 ”snapshots” as Mighell et al. (1998b), gave age ranges for certain metallicities for the clusters in their sample, which cover the ages determined in this paper.

TABLE 6
Age Comparison

Ref.Source	Lindsay 1 Gyr	Kron 3 Gyr	NGC 339 Gyr	NGC 416 Gyr	Lindsay 38 Gyr	NGC 419 Gyr
This paper	7.5 ± 0.5	6.5 ± 0.5	6 ± 0.5	6 ± 0.5	6.5 ± 0.5	$1.2 - 1.6$
Rich et al. (2000)	-	$5.6 - 7.9$	$5.0 - 7.9$	$4.0 - 7.1$	-	$1.0 - 1.8$
Mighell et al. (1998b)	7.7 ± 0.4	4.7 ± 0.7	5.0 ± 0.6	5.6 ± 0.6	-	-
Udalski (1998)	9.0	7.5	4.0	6.6	-	3.3
Sarajedini et al. (1995)	7.3 ± 0.6	-	-	-	-	-
Alcaino et al. (1996, 2003)	$9 - 10$	8	-	-	-	-
Piatti et al. (2001)	-	-	-	-	6.0 ± 0.6	-

[a] Comparison of our ages derived with the Dartmouth isochrones. For NGC 419 Padova isochones provided the best fit.

The ages published by Udalski (1998) using OGLE (Optical Gravitational Lensing Experiment) data, do not exhibit a general trend to older or younger ages as compared to our results, and the age difference varies for each cluster. The OGLE survey is a shallow ground-based survey with a limiting magnitude of ∼21 mag. Sarajedini et al. (1995) used the B-V color difference between the HB and the RGB for star clusters with red HB morphologies for their age determination. The CMDs were obtained using data from the 2048 RCA prime-focus CCD on the CTIO 4 m telescope (Olszewski et al. 1987) and the photometry reaches V∼23 mag. The age found for Lindsay 1 is in excellent agreement with our result.

Alcaino et al. (1996, 2003) used photometry for Lindsay 1 obtained with the 1.3 m Warsaw telescope, Las Campanas Observatory and reaches V∼22 mag. The age was determined by using the so-called vertical method, based on the difference between the luminosity of the MSTO and the HB level. For Kron 3, the photometry was taken with the EFOSC-2 CCD camera at the 2.2 m Max-Planck-Institute telescope of ESO , La Silla, and reaches V∼23 mag (Alcaino et al. 1996). The age was determined using isochrones. In both studies, the resulting ages are higher than our values. Piatti et al. (2001) were the first to publish an age for Lindsay 38, which is in excellent agreement with the age derived in this paper.

Most CMDs published in previous studies do not go deep enough to show a clearly outlined MSTO, which is an essential feature for most age determination techniques. Mighell et al. (1998b) determined their cluster ages relative to the age of Lindsay 1, measuring the difference between the RC and the RGB and found similar ages as in this paper. Kron 3 is an exception for which the authors derived a younger age due to large error associated with the MS photometry. Rich et al. (2000) fitted isochrones to the red clump and also calculated the difference between the MSTO and the RC (ΔV_{TO}^{RC}) in combination with the calibration of Walker (1992). The cluster ages found in this paper are within the age ranges given by Rich et al. (2000). CMDs using ground-based photometry reach ∼V=20 mag, which is not deep enough to show the SGBs or the MSTOs, which can lead to large age differences.

7.2. *Age range and spatial distribution*

The intermediate-age SMC star clusters Lindsay 1, Kron 3, NGC 339, NGC 416, and Lindsay 38 form a continuous age sequence from 6 to 7.5 Gyr. The SMC is the only dwarf galaxy of the Local Group known to contain populous star clusters in this age range. The only "true" globular cluster in the SMC, NGC 121, has an age of 10.5-11.5 Gyr (Paper I), but is still 2-3 Gyr younger than the oldest LMC and MW globular clusters (e.g., Olszewski et al. 1996; Olsen et al. 1998; Johnson et al. 1999; Mackey & Gilmore 2004). Between NGC 121, and the second oldest cluster, Lindsay 1, there is a small age-gap (∼3 Gyr), in which no surviving star cluster has been formed.

In our sample, we have four clusters with ages between 6-6.5 Gyr, and one that is significantly younger (1.2-1.6 Gyr). Good quality ages are available from ground-based and space-based observations for ten additional intermediate-age SMC star clusters. Combining them with our star clusters, we obtain a complete sample of all intermediate-age and old SMC star clusters: Kron 28, Kron 44, Lindsay 116, Lindsay 32, Lindsay 11, NGC 152, NGC 361, NGC 411, Lindsay 113, and BS90 (Table 7).

For none of these clusters deep HST photometry is available, thus their ages should be considered with some caution. For NGC 152, NGC 361, NGC 411, Lindsay 113, and BS90 "snapshots" are available taken with WFPC2 (reaching V∼23 mag), and ACS (BS90, reaching V∼26 mag).

Looking at Figure 1, we clearly see that the youngest clusters are located near the SMC main body, while the clusters with ages higher than ∼4 Gyr lie in the outer parts. NGC 361 seems to be an exception, but the cluster age is still uncertain, and the literature age of 8.1 Gyr probably is too high. Crowl et al. (2001) determined a distance of 51.7 ± 1.8 kpc for N361 whereby the cluster lies ∼ 7.5 kpc ahead of the SMC center. Another exception is BS90 that lies near the SMC main body, even though the cluster has an age of ∼4.3 Gyr. The three oldest SMC clusters (NGC 121, Lindsay 1, Kron 3) are located in the north-western part of the SMC. We note that Lindsay 116 cannot be seen in Figure 1, because it is located 6°.1 south-east of the bar and lies therefore outside the displayed area.

The closest cluster in our sample, NGC 419, and the farthest cluster, Lindsay 38, have a relative radial distance of 17 kpc from each other. We can therefore confirm that the SMC has a large extension along the line-of-sight, as was also found by Crowl et al. (2001) based on its star clusters.

In Figure 43 we show the distribution of age vs the distance to the sun of the clusters in our sample. The locations are shown relative to our adopted SMC distance and indicate that the clusters generally are distributed

TABLE 7
LITERATURE CLUSTER AGES

Cluster	Age Gyr	Data	Method	Ref.Source
Kron 28	2.1 ± 0.5	CTIO 0.9 m telescope / Tektronix 2K # 3 CCD	$\Delta V^{RC,HB}_{MSTO}$	Piatti et al. (2001)
Kron 44	3.1 ± 0.8	CTIO 0.9 m telescope / Tektronix 2K # 3 CCD	$\Delta V^{RC,HB}_{MSTO}$	Piatti et al. (2001)
Lindsay 116	2.8 ± 1.0	CTIO 0.9 m telescope / Tektronix 2K # 3 CCD	$\Delta V^{RC,HB}_{MSTO}$	Piatti et al. (2001)
Lindsay 32	4.8 ± 0.5	CTIO 0.9 m telescope / Tektronix 2K # 3 CCD	$\Delta V^{RC,HB}_{MSTO}$	Piatti et al. (2001)
Lindsay 11	3.5 ± 1.0	CTIO 4.0 m telescope / RCA CCD	Isochrones	Mould et al. (1992)
NGC 152	1.4 ± 0.2	HST/WFPC2	Isochrones	Crowl et al. (2001)
NGC 361	8.1 ± 1.2	HST/WFPC2	Isochrones	Mighell et al. (1998b)
NGC 411	1.2 ± 0.2	HST/WFPC2	Isochrones	Alves & Sarajedini (1999)
Lindsay 113	4.0 ± 0.7	HST/WFPC2	d_{B-V} [b]	Mighell et al. (1998a)
BS90	4.3 ± 0.1	HST/ACS	Isochrones	Sabbi et al. (2007)

[b] The method used by Mighell et al. (1998a) is defined by the (B-V) color difference between the mean color of the red clump and the RGB at the level of the RGB. This value then was compared with Lindsay 1, NGC 416, and Lindsay 113.

[a] Ages for nine additional intermediate-age clusters from the literature.

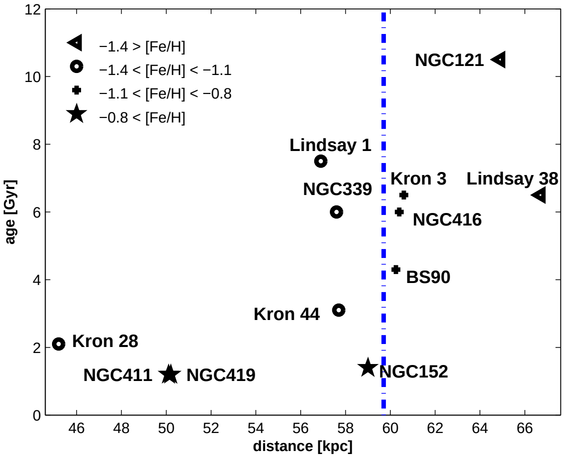

FIG. 43.— Age vs distance to the sun (projected distance) including different symbols for different metallicity ranges. For five clusters we found reliable distances Crowl et al. (2001), ages (Alves & Sarajedini 1999; Piatti et al. 2001; Crowl et al. 2001), and metallicities (Kayser et al. 2008, in prep.). All values for BS90 were adopted from Sabbi et al. (2007). The dashed line represents the SMC distance modulus of $(m-M)_0 = 18.88 \pm 0.1$ mag (Storm et al. 2004).

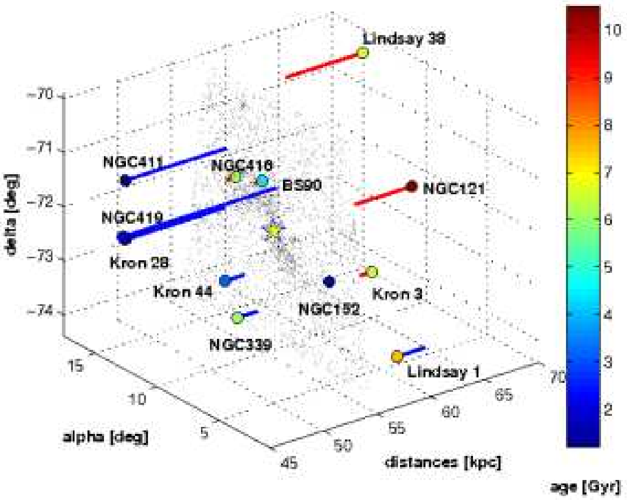

FIG. 44.— Three dimensional distribution is shown for SMC star clusters with ages and distances derived from isochrone fits to CMDs derived from HST observations. Note that the intermediate age clusters are distributed throughout much of the extended body of the SMC. As discussed in the text, the selection of clusters is biased in that our observations generally avoided clusters in locations with high field star densities. However, this incomplete sample suggests that age and radial distance from the center of the SMC are not correlated; e.g. the younger cluster Kron 28, NGC 411, and NGC 419 are at large radial distances and cover a range in metallicity. The yellow star symbolizes the SMC center.

within ±6-7 kpc of the SMC centroid. Interesting exceptions are the younger clusters Kron 28, NGC 411, and NGC 419 that in projection appear near the center of the SMC. In fact, they could be located considerably closer to us (see also Fig. 44). Further measurements of the distance of younger clusters thus would be worthwhile. Moreover, we included five clusters for which we found reliable ages, distances, and metallicities in the literature. We divided the cluster metallicities into four groups and use different symbols for each group in the plot. Even though our plot contains only 11 clusters, we can see trends in the distributions of their properties. Age and distance from the sun appear to be correlated. The closest cluster, NGC 419, is also the youngest and most metal rich cluster, while the most distant cluster, Lindsay 38, is also the most metal poor, in spite of not being the oldest cluster.

One could speculate that in regions at the outskirts of the double LMC-SMC system the star formation activity has been lower/slower than elsewhere, possibly with more unenriched gas, thus allowing for a more moderate enrichment. The oldest object, NGC 121, is not the most metal poor cluster, but the second metal poorest and the second farthest one. Its low metallicity could be the result of both a "natural" age-metallicity relation and a "distance from the system" effect.

Figure 44 illustrates the distribution of SMC star clusters with high quality distances derived from isochrone fits to CMDs derived from HST observations. This is a highly biased sample; star clusters seen in the direction of the SMC 'bar' are not preferred for these projects because of their large levels of field star contamination. The exception in this case is the cluster BS90 that was accidently included in observations of NGC 346 (see Sabbi et al. 2007). The present limited data for clusters in this project show that the SMC is quite extended along

TABLE 8
Distances

Cluster	Projected Dist. kpc	Dist. to SMC Center kpc
NGC 121	64.9 ± 1.2	8.76 ± 1.1
Lindsay 1	56.9 ± 1.0	13.28 ± 1.0
Kron 3	60.6 ± 1.1	7.19 ± 1.1
NGC 339	57.6 ± 4.1	0.73 ± 2.0
NGC 416	60.4 ± 1.9	3.94 ± 1.4
Lindsay 38	66.7 ± 1.6	6.27 ± 1.3
NGC 419	50.2 ± 2.6	10.83 ± 1.6
NGC 411	50.1 ± 1.7	11.1 ± 1.3
NGC 152	59.0 ± 1.8	5.58 ± 1.3
Kron 28	45.2 ± 1.7	14.78 ± 1.3
Kron 44	57.7 ± 1.8	4.37 ± 1.3
BS90	60.3	1.23

[a] The projected distances were calculated in this paper and adopted from Crowl et al. (2001); Sabbi et al. (2007). Using these values and the cluster coordinates, we determined the cluster distances to the SMC center ($\alpha = 0^h52^m44.8^s$, $\delta = -72°49'43''$).

the line of sight, consistent with other studies of individual stars and star clusters (see discussion in § 6). This three dimensional distribution of the clusters also demonstrates the lack of trends in cluster age or metallicity with radial distance from the center of the SMC.

7.3. *Age distribution and cluster formation history*

By combining the ages of our sample with 9 literature ages for intermediate-age SMC star clusters listed in Table 7, we obtain a well-observed sample of intermediate-age and old star clusters in the SMC. The cluster NGC 361 was excluded from the sample, because the cluster is almost certainly younger than the assumed ∼8 Gyr (Mighell et al. 1998b).

The age distribution is shown in Figure 45. In each panel we show our resulting age distribution using ages of different isochrone models (black histrograms) and the combined sample (white histograms). Since the cluster ages from the literature were derived using different data and methods, their distribution does not change.

In all three plots of Figure 45, the small age gap between ∼8 and 10 Gyr can clearly be seen. In the first panel we used ages derived with the Dartmouth isochrones. Rich et al. (2000) based on HST/WFPC2 found two brief cluster formation intervals with the oldest set 8 ± 2 Gyr ago and the second 2 ± 0.5 Gyr ago, and argued that there were gaps in between. During the older burst the clusters NGC 339, NGC 361, NGC 416, and Kron 3, and during the younger burst the clusters NGC 411, NGC 152, and NGC 419 have formed according to Rich et al. (2000).

Even though they used the same HST/WFPC2 data as Rich et al. (2000), Mighell et al. (1998b) found no evidence for such cluster formation bursts. We also find no evidence for two significant bursts of star cluster formation in our SMC age distribution, but we do see a slightly enhanced cluster formation activity around 6 Gyr. In the second and the third panel we used our derived Teramo and Padova ages, respectively. The cluster formation at 6 Gyr is even more obvious for both isochrone models than in the upper panel.

Apparently, between ∼5 and 6 Gyr no star cluster with sufficient mass to survive has formed, but if Lindsay 113 is older than the assumed 4 Gyr adopted from the literature, the cluster lies within the gap. We suggest that the SMC has formed its clusters during its entire lifetime with some epochs of more intense cluster formation activity. More detailed information about the age distribution requires additional deep observations of all remaining intermediate-age SMC star clusters.

As shown in Figure 44 there appears to be no simple relationship between cluster position and metallicity in any age range. This perhaps is to be expected given that tidal interactions may have perturbed the orbits of star clusters after they formed or provided opportunities for clusters to form at large radii, as in the present-day SMC wing. We have to emphasize that the cluster sample shown in Figure 44 is not complete. Only for 12 clusters reliable distances have been measured this far (see § 6), and these are shown in the Figure. The question of the metallicity distribution of the clusters and how this relates to age and position is more complex and beyond the scope of this paper.

7.4. *Evolutionary history of the SMC as a whole*

Looking at the metallicities of our star clusters (Tab. 9), we see that the SMC did not experience a smooth age-metallicity relation, even though the SMC is believed to be well-mixed at the present day (but see Grebel & Richtler 1992; Gonzalez & Wallerstein 1999). The oldest SMC star cluster, NGC 121, has a metallicity of [Fe/H] = −1.46 ± 0.10 and an age of 10.5-11.5 Gyr, while Lindsay 38 is more metal-poor with [Fe/H] = −1.59 ± 0.10 but has an age of 6.5 ± 0.5 Gyr. SMC star clusters of similar age may differ by several tenths of dex in metallicity (see also Da Costa et al. 1998, Kayser et al. 2008, in preparation). The probably most reasonable explanation involves the infall of unenriched, or less enriched gas. The Magellanic Clouds are surrounded by an extensive HI halo (e.g., Dickey 1996), therefore this possibility may be plausible. Another speculative explanation for the existence of those metal-poor clusters is that the SMC acquired these clusters in a past interaction with another dwarf galaxy, similar to the clusters from the Sagittarius dwarf galaxy being acquired by the Milky Way (e.g., Carraro et al. 2007).

The SMC, LMC, and MW form an interacting triple system, which affects each other's star formation history (SFH). However, recent studies have suggested that the Magellanic Clouds only entered the vicinity of the MW fairly recently (e.g., Kallivayalil et al. 2006a/b). It is intriguing that the LMC has a significant age gap between ∼4-9 Gyr, while the SMC formed its clusters continuously during the same time period. Moreover, the SMC appears to have a "delayed" globular cluster formation history and formed its first and only globular cluster, NGC 121, 2-3 Gyr later then the LMC or the MW.

Possible orbits of the SMC, LMC, and MW have been modelled by several authors (e.g., Kallivayalil et al. 2006a/b; Bekki & Chiba 2005). Strong tidal perturbations due to interactions could have triggered the cluster formation (e.g., Whitmore 1999) in the SMC. In the LMC, we find that star clusters have formed in evident bursts. The LMC has two main epochs of cluster formation (e.g., Bertelli et al. 1992) and a well-known age-gap of several billion years, in which no star clusters have formed. A few globular clusters are found

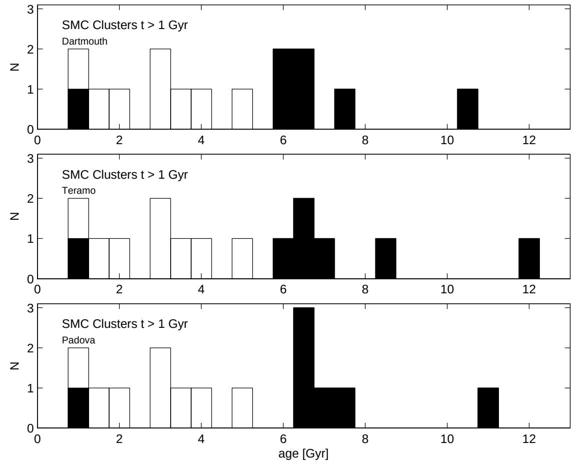

FIG. 45.— The age distribution of 15 intermediate-age and old SMC clusters (excluding NGC 361) with ages derived in this paper, in Paper I (plotted as black histograms), and adopted from (Mighell et al. 1998a/b, Mould et al. 1992; Alves & Sarajedini 1999; Rich et al. 2000; Piatti et al. 2001; Crowl et al. 2001) (plotted as white histrograms). Since the cluster ages from the literature were derived using different data and methods, their distribution does not change. In the first panel we used the ages found using the Dartmouth models, in the second we use the Padova ages, and in the last panel the Teramo ages were used. The literature ages of NGC 152, NGC 411, and Lindsay 113, are based on HST/WFPC2 data (Mighell et al. 1998a/b, Alves & Sarajedini 1999; Rich et al. 2000), while the adopted ages of Kron 28, Kron 44, Lindsay 11, Lindsay 32, and Lindsay 116 are derived from ground-based photometry (Mould et al. 1992; Crowl et al. 2001; Piatti et al. 2001). NGC 361 is not considered due to its uncertain age. The age distribution illustrates the continuous cluster formation with the small age gap between ∼8 and 10 Gyr.

with coeval ages like the Galactic globular clusters (e.g., Olszewski et al. 1991; Olsen et al. 1998; Johnson et al. 1999). We know only of one star cluster, ESO 121-SC03, that lies within the age-gap, which has an age of 8.3-9.8 Gyr (Mackey et al. 2006). A correlation between young star clusters in the LMC and putative close encounters with the SMC and MW have been found by e.g. Girardi et al. (1995), although the most recent proper motion measurements indicate that the Magellanic Clouds are currently on their first passage around the MW.

For young SMC clusters a relation between close encounters and the cluster formation history is not as obvious as for LMC clusters probably due to a smaller number of clusters (Chiosi et al. 2006). The age distribution in Figure 45 shows that a slightly enhanced number of star clusters with ages around 1 Gyr is located in the SMC, which might have been produced through a cloud-cloud collision after a pericenter passage ∼0.5 Gyr ago (Bekki & Chiba 2005). But evidently massive star clusters older than 1 Gyr have formed continuously until ∼7.5 Gyr ago (Lindsay 1). It is not yet understood why populous star clusters older than 4 Gyr have not formed and survived continuously in the LMC, while in the SMC they did. Bekki & Chiba (2005) explained the different cluster formation histories of the Clouds as a difference in birth locations and initial mass of the host galaxies.

Kallivayalil et al. (2006a/b, see also Piatek et al. 2008) measured proper motions for the SMC and the LMC and used Monte Carlo simulations to model the orbits of the Clouds and the MW. While they found bound orbits for the Clouds, they also found that it was difficult to keep the Clouds bound to each other for more than 1 Gyr in the past. It is possible that the Clouds are not a bound system (see also e.g., Bekki & Chiba 2005), and that they are making their first passage close to the Milky Way.

8. SUMMARY

In this paper, we have presented ages for the six intermediate-age SMC star clusters Lindsay 1, Kron 3, NGC 339, NGC 416, Lindsay 38, and NGC 419 based on HST/ACS stellar photometry in the F555W and F814W passbands. The resulting CMDs represent the deepest published photometry so far and extend at least three magnitudes below the respective MSTOs. In order to obtain absolute ages, we applied three different isochrone models. The resulting ages are summarized in Table 9. We list the clusters by their identification in column (1). The [Fe/H] values are given in column (2) in the scale by Zinn & West (1984). Column (3) shows the magnitude of the MSTO $m_{555,TO}$, column (4) the magnitude of the red bump and column (5) the magnitude of the red clump $m_{555,RC}$. The columns (6), (7) and (8) show the absolute ages determined using the isochrone models of Teramo, Padova and Dartmouth.

We find that the Dartmouth isochrones provide the closest approximation to the MS, SGB, and RGB, whereas the other models mostly cannot reproduce the slope of the upper RGB when using the spectroscopically determined metallicity and requiring that the isochrones fit the MSTO and SGB. The Dartmouth isochrone models yield ages of 7.5±0.5 for Lindsay 1, 6.5±0.5 for Kron 3, 6 ± 0.5 for NGC 339, 6 ± 0.8 for NGC 416, and 6.5 ± 0.5 for Lindsay 38. In general the isochrones provide good fits to the MSTO and SGBs that determine ages.

For the youngest cluster, NGC 419, only the Padova isochrones fitted the CMD, while the Teramo isochrones had major problems with fitting the SGB and RGB, and the Dartmouth isochrones are not available for such young ages.

The difficulties of various isochrone models of given metallicities in reproducing the upper red giant branches of clusters with the same metallicities are a well-known problem (e.g., Grebel 1997, 1999). Figures 18, 22, and 30 reflect the general failure of the chosen stellar evolutionary models to simultaneously reproduce all of the major features of CMDs (e.g., Gallart et al. 2005) in spite of the excellent fit to the lower RGB, SGB, and MS. For each cluster we fitted a fiducial ridgeline that provides a unique set of low-metallicity fiducial isochrones, which are invaluable for detailed comparisons with stellar evolution models.

In each of our cluster CMDs stars blueward of and above the MSTOs are visible, which could be BSS. The radial cumulative distribution of BSS candidats in Lindsay 1, Kron 3, NGC 339, Lindsay 38, and NGC 419 showed that the stars found in the BSS regions are not concentrated toward the cluster centers and are therefore most probably part of the younger MS of the SMC field star population. For NGC 416, we find an indication for centrally concentrated BSS candidates.

Looking at the spatial distribution, we find that the three oldest SMC clusters (NGC 121, Lindsay 1, Kron 3) lie in the north-western part of the SMC, while the

TABLE 9
PARAMETERS

Cluster	$[Fe/H]_{ZW84}$	Age_{Teramo} Gyr	Age_{Padova} Gyr	$Age_{Dartmouth}$ Gyr
NGC 121	-1.46 ± 0.10	11.8 ± 0.7	11.2 ± 0.7	10.5 ± 0.5
Lindsay 1	-1.14 ± 0.10	8.3 ± 0.7	7.7 ± 0.7	7.5 ± 0.5
Kron 3	-1.08 ± 0.12	7.2 ± 0.5	7.1 ± 0.7	6.5 ± 0.5
NGC 339	-1.12 ± 0.10	6.6 ± 0.5	6.3 ± 0.5	6 ± 0.5
NGC 416	-1.00 ± 0.13	6 ± 0.8	6.6 ± 0.8	6 ± 0.8
Lindsay 38	-1.59 ± 0.10	6.3 ± 0.5	6.3 ± 0.5	6.5 ± 0.5
NGC 419	-0.67 ± 0.12		1.2-1.6	1.2-1.6

[a] All derived ages are listed. The metallicities for the clusters NGC 121, Lindsay 1, Kron 3 and NGC 339 are taken from Da Costa & Hatzidimitriou (1998), where we adopted the ZW84 metallicity scale. The metallicities for NGC 416, Lindsay 38, and NGC 419, were taken from Kayser et al. 2008, in prep. in the CG97 scale, and which we transformed to ZW84 scale by using the transformation by Carretta & Gratton (1997).

youngest clusters are located near the SMC main body. Star clusters with ages higher than ∼4 Gyr are located in the outer parts.

From the observed red clump magnitude we give a distance estimate for our clusters. We find that Lindsay 38 is the most distant cluster in our sample with d∼68 kpc, while NGC 419 is the closest cluster with d∼53 kpc. Therefore, the closest and farthest cluster in our sample have a distance from each other of ∼17 kpc, which agrees with the assumed large depth extent of the SMC.

Further, we conclude that the SMC experienced massive cluster formation, remnants of which have survived from over much of its lifetime, unlike the LMC or MW. The oldest and only globular cluster, NGC 121, has formed ∼11 Gyr ago, while the next oldest set of surviving massive clusters, e.g. Lindsay 1 or NGC 361, date from approximately 3 Gyr later. After this time the largest age gaps are ∼1 Gyr suggesting that massive star clusters occured without any substantial multi-Gyr hiatus. The SMC apparently formed massive star clusters that have survived from most of its lifetime.

We would like to thank an anonymous referee for his or her useful comments. We gratefully acknowledge support by the Swiss National Science Foundation through grant number 200020-105260 and 200020-113697. Support for the US component of this program GO-10396 was provided by NASA through a grant from the Space Telescope Science Institute, which is operated by the Association of Universities for Research in Astronomy, Inc., under NASA contract NAS 5-26555. We warmly thank Paolo Montegriffo to provide his software and Leo Girardi for the Padova isochrones in the standard ACS color system. Gisella Clementini and Monica Tosi have been partially supported by PRIN-MIUR-2004 and PRIN-INAF-2005, and Jay Gallagher also obtained helpful additional support from the University of Wisconsin Graduate School and from the Heidelberg Graduate School of Fundamental Physics.

REFERENCES

Alcaino, G., Liller, W., Alvarado, F., Kravtsov, V., Ipatov, A., Samus, N., & Smirnov, O. 1996, AJ, 112, 2004
Alcaino, G. 2003, A&A, 407, 919
Alves, D. R., & Sarajedini, A. 1999, ApJ, 511, 225
Alves, D. R. 2004, New Astronomy Review, 48, 659
Bailyn, C. D. 1995, ARA&A, 33, 133
Bekki, K., & Chiba, M. 2005, MNRAS, 356, 680
Bellazzini, M., Fusi Pecci, F., Messineo, M., Monaco, L., & Rood, R. T. 2002, AJ, 123, 1509
Bertelli, G., Mateo, M., Chiosi, C., & Bressan, A. 1992, ApJ, 388, 400
Bertin, E., & Arnouts, S. 1996, A&AS, 117, 393
Bica, E., Dottori, H., Pastoriza, M. 1985, A&A, 156, 261
Buonanno, R., Corsi, C. E., Fusi Pecci, F., Richer, H. B., & Fahlman,G. G. 1995, AJ, 109, 650
Carraro, G., Zinn, R., & Moni Bidin, C. 2007, A&A, 466, 181
Carraro, G., Vazquez, R. A., & Moitinho, A. 2008, ArXiv e-prints, 802, arXiv:0802.3557
Carretta, E., & Gratton, R. G. 1997, A&AS, 121, 95
Chiosi, E., Vallenari, A., Held, E. V., Rizzi, L., & Moretti, A. 2006, A&A, 452, 179
Crowl, H. H., Sarajedini, A., Piatti, A. E., Geisler, D., Bica, E., Clariá, J. J., & Santos, J. F. C., Jr. 2001, AJ, 122, 220
Da Costa, G. S. & Hatzidimitriou, D. 1998, AJ, 115, 1934
Da Costa, G. S. 2002, in IAU Symp. 207, Extragalactic Star Clusters, ed. D. Geisler, E. K. Grebel, & D. Minitti (San Francisco: ASP), 83
De Angeli, F., Piotto, G., Cassisi, S., Busso, G., Recio-Blanco, A., Salaris, M., Aparicio, A., & Rosenberg, A. 2005, AJ, 130, 116
Dean, J. F., Warren, P. R., & Cousins, A. W. J. 1978, MNRAS, 183, 569
Dickey, J. M. 1996, The Minnesota Lectures on Extragalactic Hydrogen, ed. E. D. Skillman (San Francisco: ASP), 106, p. 187
Dotter, A., Chaboyer, B., Jevremović, D., Baron, E., Ferguson, J. W., Sarajedini, A., & Anderson, J. 2007, AJ, 134, 376
Durand, D., Hardy, E., Melnick, J. 1984, AJ, 283, 552
Dutra, C., M., Bica, E., Clariá, J. J., Piatti, A. E. 1999, MNRAS, 305, 373
Elson, R. A. W., & Fall, S. M. 1985, AJ, 299, 211
Ferraro, F. R., Sills, A., Rood, R. T., Paltrinieri, B., & Buonanno, R. 2003, ApJ, 588, 464
Fusi Pecci, F., Bellazzini, M., Cacciari, C. & Ferraro F. R. 1995, AJ, 110, 1664
Gallart, C., Zoccali, M., & Aparicio, A. 2005, ARA&A, 43, 387
Gascoigne, S. C. B. 1966, MNRAS, 134, 59
Gascoigne, S. C. B. 1980, Star clusters, ed. by J. E. Hesser (Reidel Dordrecht), IAU Symp., 85, 305
Gieles, M., Lamers, H. J. G. L. M., & Portegies Zwart, S. F. 2007, ApJ, 668, 268
Girardi, L., Chiosi, C., Bertelli, G., & Bressan, A. 1995, A&A, 298, 87
Girardi, L., Bressan, A., Bertelli, G., & Chiosi, C. 2000, A&AS, 141, 371
Girardi, L., & Salaris, M. 2001, MNRAS, 323, 109

Glatt, K., et al. 2008, AJ, 135, 1106

Gonzalez, G., & Wallerstein, G. 1999, AJ, 117, 2286

Grebel, E. K., & Richtler, T. 1992, A&A, 253, 359

Grebel, E. K., Roberts, W. J., & Brandner, W. 1996, A&A, 311, 470

Grebel, E. K. 1997, Reviews in Modern Astronomy, 10, 27

Grebel, E. K. 1999, The Stellar Content of the Local Group, IAU Symp. 192, eds. P. Whitelock & R. Cannon (San Francisco: ASP), 17

Grebel, E. K., & Gallagher, J. S., III 2004, ApJ, 610, L89

Harris, J., & Zaritsky, D. 2001, ApJS, 136, 25

Hatzidimitriou, D., Cannon, R. D., & Hawkins, M. R. S. 1993, MNRAS, 261, 873

Holtzman, J. A. 1999, AJ, 118, 2262

Hunter, D. A., Elmegreen, B. G., Dupuy, T. J., & Mortonson, M. 2003, AJ, 126, 1836

Johnson, J. A. Bolte, M., Stetson, P. B., Hesser, J. E., & Somerville, R. S. 1999, ApJ, 527, 199

Kallivayalil, N., van der Marel, R. P., Alcock, C., Axelrod, T., Cook, K. H., Drake, A. J., & Geha, M. 2006a, ApJ, 638, 772

Kallivayalil, N., van der Marel, R. P., & Alcock, C. 2006b, ApJ, 652, 1213

Kayser, A., Grebel, E. K., Harbeck, D. R., Cole, A. A., Koch, A., Gallagher, J. S., & Da Costa, G. S. 2006, ArXiv Astrophysics e-prints, arXiv:astro-ph/0607047

Kayser, A., Grebel, E. K., Harbeck, D. R., Cole, A. A., Koch, A., Glatt, K., Gallagher, J. S., & Da Costa, G. S. 2007, Stellar Populations as Building Blocks of Galaxies, IAU Symp. 241, eds. A. Vazdekis & R. F. Peletier (Cambridge: Cambridge University Press), 351

Koekemoer, A. M., Fruchter, A. S., Hook, R. N., & Hack, W. 2002, in *Hubble* after the Installation of the ACS and the NICMOS Cooling System, ed. S. Arribas, A. Koekemoer & B. Whitmore (Baltimore: STScI), 337

Kron, G. E. 1956, PASP, 68, 125

Lah, P., Kiss, L. L., & Bedding, T. R. 2005, MNRAS, 359, L42

Lamers, H. J. G. L. M., Gieles, M., & Portegies Zwart, S. F. 2005, A&A, 429, 173

Lindsay, E. M. 1958, MNRAS, 118, 172

Mackey, A. D. & Gilmore, G. F. 2004, MNRAS, 352, 153

Mackey, A. D., Payne, M. J., & Gilmore, G. F. 2006, MNRAS, 369, 921

Mackey, A. D., & Broby Nielsen, P. 2007, MNRAS, 379, 151

Mackey, A. D., Broby Nielsen, P., Ferguson, A. M. N., & Richardson, J. C. 2008, ArXiv e-prints, 804, arXiv:0804.3475

Mathewson, D. S., Ford, V. L., & Visvanathan, N. 1988, ApJ, 333, 617

Mighell, K. J., Sarajedini, A., & French, R. S. 1998, ApJ, 494, L189

Mighell, K. J., Sarajedini, A. & French, R. S. 1998, AJ, 116, 2395

Mould, J. R., Jensen, J. B., & Da Costa, G. S. 1992, ApJS, 82, 489

Olsen, K. A. G., Hodge, P. W., Mateo, M., Olszewski, E. W., Schommer, R. A., Suntzeff, N. B., & Walker, A. R. 1998, MNRAS, 300, 665

Olszewski, E.W. 1987, AJ, 93, 565

Olszewski, E. W., Schommer, R. A., Suntzeff, N. B., & Harris, H. C. 1991, AJ, 101, 515

Olszewski, E. W., Suntzeff, N. B., & Mateo, M. 1996, ARA&A, 34, 511

Piatek, S., Pryor, C., & Olszewski, E. W. 2008, AJ, 135, 1024

Piatti, A. E., Santos, J. F. C., Clariá, J. J., Bica, E., Sarajedini, A.& Geisler, D. 2001, MNRAS, 325, 792

Pietrinferni, A., Cassisi, S., Salaris, M. & Castelli, F. 2004, AJ, 612, 168

Ratnatunga, K. U., & Bahcall, J. N. 1985, ApJS, 59, 63

Rich, R. M., Da Costa, G. S., & Mould, J. R. 1984, ApJ, 286, 517

Rich, R. M., Shara, M., Fall, S. M., & Zurek, D. 2000, AJ, 119, 197

Rosenberg, A., Saviane, I., Piotto, G., Aparicio, A. & Zaggia, S. R. 1998, AJ, 115, 648

Sabbi, E., et al. 2007, AJ, 133, 44

Salaris, M., & Girardi, L. 2002, MNRAS, 337, 332

Sarajedini, A., Lee, Y.-W. & Lee, D.-H. 1995, ApJ, 450, 712

Sarajedini, A. 1999, AJ, 118, 2321

Schaller, G., Schaerer, D., Meynet, G., & Maeder, A. 1992, A&AS, 96, 269

Schlegel, D. J., Finkbeiner, D. P., & Davis, M. 1998, ApJ, 500, 525

Shapley, H., & Wilson, H. H. 1925, Harvard College Observatory Circular, 276, 1

Shara, M. M., Fall, S. M., Rich, R. M., & Zurek, D. 1998, ApJ, 508, 570

Sirianni, M. 2005, PASP, 117, 1049

Storm, J., Carney, B. W., Gieren, W. P., Fouqué, P., Latham, D. W., & Fry, A. M. 2004, A&A, 415, 531

Suntzeff, N. B., Olszewski, E. W. & Walker, A. R. 1992, AJ, 104, 1743

Udalski, A. 1998, Acta Astronomica, 48, 383

Walker, A. R. 1992, ApJ, 390, 81

Whitmore, B. C. 1999, in IAU Symp. 186, Galaxy Interactions at Low and High Redshift, ed. J. E. Barnes & D. B. Sanders (Dordrecht: Kluwer), 251

Yoshizawa, A.M. & Noguchi, M. 2003, MNRAS, 339, 1135

Zaritsky, D., Harris, J., Thompson, I. B., Grebel, E. K., & Massey, P. 2002, AJ, 123, 855

Zinn, R., & West, M. J.1984, ApJS, 55, 45

Zinn, R. 1993, The Globular Cluster-Galaxy Connection, ASP Conf. Ser. 48, eds. Smith, G. H. & Brodie, J. P. (San Francisco: ASP), 302